



Michigan Technological University  
*Create the Future* Digital Commons @ Michigan Tech

---

Dissertations, Master's Theses and Master's  
Reports - Open

Dissertations, Master's Theses and Master's  
Reports

---

2011

## Numerical modeling of the failure mechanisms in Si thin film anode for Li-ion batteries

Siddharth H. Patel  
*Michigan Technological University*

Follow this and additional works at: <https://digitalcommons.mtu.edu/etds>

 Part of the [Mechanical Engineering Commons](#)

Copyright 2011 Siddharth H. Patel

---

### Recommended Citation

Patel, Siddharth H., "Numerical modeling of the failure mechanisms in Si thin film anode for Li-ion batteries", Master's Thesis, Michigan Technological University, 2011.  
<https://doi.org/10.37099/mtu.dc.etds/396>

Follow this and additional works at: <https://digitalcommons.mtu.edu/etds>

 Part of the [Mechanical Engineering Commons](#)

NUMERICAL MODELING OF THE FAILURE MECHANISMS IN SI THIN FILM  
ANODE FOR LI-ION BATTERIES

By

Siddharth H. Patel

A THESIS

Submitted in partial fulfillment of the requirements for the degree of

MASTER OF SCIENCE

(Mechanical Engineering)

MICHIGAN TECHNOLOGICAL UNIVERSITY

2011

© 2011 Siddharth H. Patel

This Thesis, “Numerical Modeling of the Failure Mechanisms in Si Thin Film Anode for Li-ion Batteries,” is hereby approved in partial fulfillment of the requirements for the Degree of MASTER OF SCIENCE IN MECHANICAL ENGINEERING.

Department of Mechanical Engineering-Engineering Mechanics

Signatures:

Thesis Co-Advisor

\_\_\_\_\_  
Dr. Spandan Maiti

Thesis Co-Advisor

\_\_\_\_\_  
Dr. Gregory M. Odegard

Committee Member

\_\_\_\_\_  
Dr. Stephen A. Hackney

Department Chair

\_\_\_\_\_  
Dr. William W. Predebon

Date

\_\_\_\_\_

# Table of Contents

<b>List of Figures</b> .....	v
<b>List of Tables</b> .....	vii
<b>Abstract</b> .....	viii
<b>1. Introduction</b> .....	1
<b>2. Literature Review</b> .....	6
2.1. Experimental Studies .....	6
2.1.1. Silicon Thin film.....	7
2.1.2. Silicon Nano-Composites.....	9
2.2. Numerical Models.....	11
2.2.1. Numerical studies of single particle electrode for stress evolution.....	12
2.2.2. Numerical studies on Thin film electrodes with the overall battery performance.....	14
2.2.3. Models presenting various related phenomena affecting electrode performance.....	15
2.3. Research Objective .....	16
<b>3. Computational Framework</b> .....	17
3.1. Continuum modeling of the diffusion induced expansion.....	17
3.1.1. Kinematic of diffusion induced expansion.....	17
3.1.2. Balance equations and constitutive relations.....	19
3.2. Computational modeling of lithium intercalation and stress generation .....	22
3.2.1. Operator split technique .....	23
3.2.2. Variational form and linearization.....	23
3.2.3. Solution strategy.....	27

3.3. Modeling of plastic deformation in current collector .....	27
3.4. Cohesive zone Model for Crack propagation .....	29
3.4.1. Finite Element Implementation .....	32
3.5. Verification of the Numerical Framework.....	33
3.5.1. Diffusion in the Semi-infinite region .....	33
3.5.2. Bending of Bimetallic strip under thermal loading .....	36
<b>4. Results &amp; Discussion .....</b>	<b>39</b>
4.1. Problem description .....	39
4.2. Li-ion intercalation process.....	42
4.3. Effect of interfacial material properties on crack initiation.....	45
4.4. Effect of substrate material properties on crack initiation .....	47
4.5. Effect of the plasticity on crack initiation.....	48
<b>5. Conclusion and Future work .....</b>	<b>54</b>
5.1. Conclusions.....	54
5.2. Future recommendations.....	55
<b>6. Bibliography .....</b>	<b>56</b>
<b>7. Appendix.....</b>	<b>62</b>

# List of Figures

1.1	Basic structure of the lithium-ion electrochemical cell during discharging. ....	2
1.2	Li-ion migration during charging and discharging of Li-ion battery with graphite anode and $\text{LiCoO}_2$ .....	3
1.3	Publication related to anode materials for Li-ion battery.....	4
2.1	Si-Thin film (a) Specific capacity comparison based on cycling rate (b) SEM Morphology of Si thin film on Cu-substrate after 30 cycles.....	7
2.2	The gravimetric capacity of the ballistically deposited silicon nanocrystals and the a-silicon nanofilm over 50 cycles, compared with the capacity of graphite ( $\text{LiC}_6$ ) and bulk silicon.....	8
2.3	Specific capacity over the period of 30 cycles for graphene, nanosize Si, Si/graphene composite electrodes, and calculated pure Si contribution from Si/graphene composite.....	11
2.4	Comparison of results showing Hydrostatic stress effect.....	12
3.1	Graphical representations for multiplicative decomposition of Intercalation induced deformation gradient.....	19
3.2	Representative volume with cohesive surface.....	30
3.3	Loading/unloading path for traction-separation law.....	31
3.4	Semi infinite bar with applied boundary conditions at $x = 0$ .....	33
3.5	Verification of case 1 with fixed Concentration ( $C_0$ ) at $x = 0$ .....	35
3.6	Verification of case 2 with fixed flux ( $J_0$ ) at $x = 0$ .....	35
3.7	Bimetallic strip with applied temperature at top and bottom surfaces.....	36
3.8	Bimetallic strip comparison of deformed and undeformed configuration. ....	38
4.1	Si-island subjected to Li-ion flux, attached to current collector. Structure has a fixed support at the bottom.....	40
4.2	Symmetric portion of the domain considered for the simulation.....	42
4.3	Li-ion concentration profile during Lithiation cycle at 1C-rate.....	43

4.4	Li-ion concentration profile during Delithiation cycle at 1C-rate.....	43
4.5	Comparison of deformed and undeformed conditions at the end of the lithiation cycle.....	44
4.6	Comparison of deformed and undeformed conditions at the end of the delithiation cycle.....	44
4.7	Time of crack initiation for various cohesive toughness ( $G_c$ ) and cohesive strength ( $\sigma_c$ ) considering constant elastic modulus of substrate $E = 100$ GPa.....	45
4.8	Buckling of the Si-island because of the intercalation induced volume expansion during lithiation cycle.....	46
4.9	Time of crack initiation for various elastic moduli ( $E$ ) of substrate and cohesive toughness ( $G_c$ ) considering constant cohesive strength ( $\sigma_c$ ) = 1 GPa.....	47
4.10	Time of crack initiation for various elastic moduli ( $E$ ) of substrate and cohesive strength ( $\sigma_c$ ) considering constant cohesive toughness $G_c = 20$ J/m <sup>2</sup> . ....	48
4.11	Comparison of plasticity effect on crack initiation time for various cohesive strengths ( $\sigma_c$ ), considering constant cohesive toughness $G_c = 10$ J/m <sup>2</sup> and constant Elastic modulus of substrate $E = 100$ GPa. ....	49
4.12	Comparison of failure mode during Lithiation and Delithiation cycles.....	50
4.13	Comparison of plasticity effect on crack initiation time for various Elastic modulus of substrate $E$ , considering constant cohesive toughness $G_c = 20$ J/m <sup>2</sup> and constant cohesive strength $\sigma_c = 2$ GPa.....	51
4.14	Comparison of plasticity effect on crack initiation time for various cohesive toughness ( $G_c$ ), considering constant Elastic modulus of substrate $E = 100$ GPa and constant cohesive strength $\sigma_c = 2$ GPa.....	51
4.15	Comparison of tensile stress generated at the middle of the Si-island considering the plasticity effect.....	52
4.16	Comparison of tensile stress generated at the corner of the Si-island considering the plasticity effect.....	53

# List of Tables

1.1	Lithiated phases and Intercalation capacity of different materials.....	3
3.1	Material variables and dimensions used for the simulation.....	37
3.2	Comparison of Simulation results with analytical for deflection at the free end of bimetallic strip.....	38
4.1	Input data required for the Numerical simulation.....	41
4.2	Material data for Si thin film used in the simulations.....	41



# Abstract

In recent times, the demand for the storage of electrical energy has grown rapidly for both static applications and the portable electronics enforcing the substantial improvement in battery systems, and Li-ion batteries have been proven to have maximum energy storage density in all rechargeable batteries. However, major breakthroughs are required to consummate the requirement of higher energy density with lower cost to penetrate new markets. Graphite anode having limited capacity has become a bottle neck in the process of developing next generation batteries and can be replaced by higher capacity metals such as Silicon. In the present study we are focusing on the mechanical behavior of the Si-thin film anode under various operating conditions. A numerical model is developed to simulate the intercalation induced stress and the failure mechanism of the complex anode structure. Effect of the various physical phenomena such as diffusion induced stress, plasticity and the crack propagation are investigated to predict better performance parameters for improved design.

# Chapter 1

## Introduction

Lithium ion batteries have drawn continuous commercial interest since its introduction by Sony in 1991 followed by cathode research by John Goodenough and his team. Because of the advantages like high energy density, no memory effect and high open circuit voltage, Li-ion batteries have become first choice for the consumer electronics such as cellular phones, cameras, laptops computers, etc. However, despite its commercial success, major improvements are required in terms of cost, safety and energy density for the uses such as in hybrid and electric vehicles. New materials and configurations are being developed constantly to improve the performance of these batteries.

It is very important to first understand basic structure and chemical processes associated with lithium-ion batteries. Electrochemical cell, the smallest working-unit of the battery, contains electrodes (anode and cathode), current collectors, electrolyte, and separator as shown in Figure. 1.1.

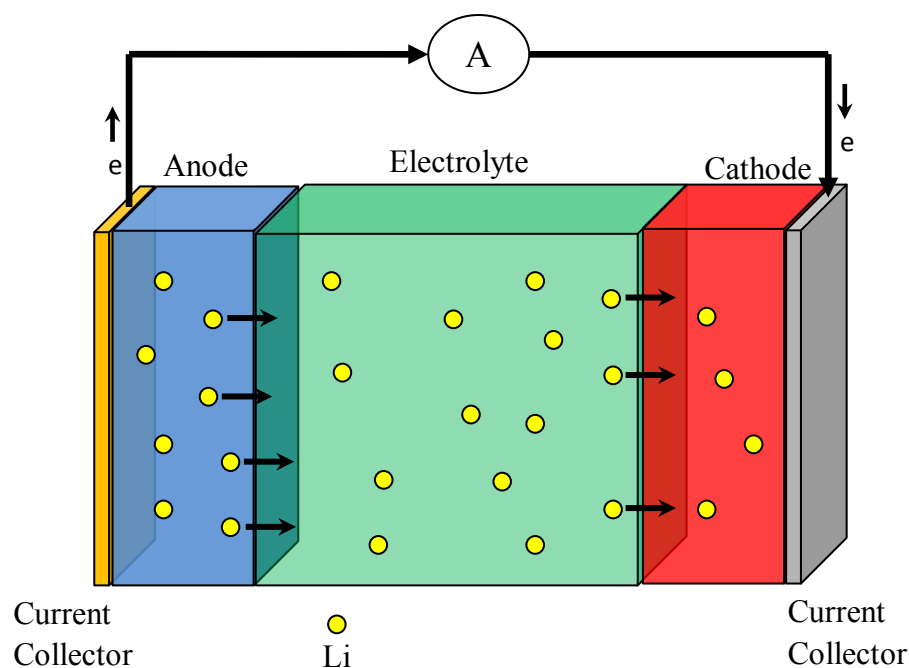
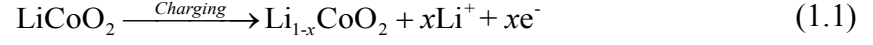


**Figure 1.1:** Basic structure of the lithium-ion electrochemical cell during discharging.

During discharge Li-ions diffuse out of the anode and migrate to cathode through electrolyte while associated electrons travel through electrical circuit to perform external work. Most Common material used as anode is graphite. Cathode is a positive electrode and absorbs lithium ions through electrolyte and electrons through outer circuit during discharging. Lithium metal oxides (i.e.  $\text{LiCoO}_2$  and  $\text{LiMn}_2\text{O}_4$ ) are commonly used cathode material. As the name suggests, current collector attached to the active electrode material carries electrons to and from outer circuit. Metals like copper and aluminum are commonly used as current collectors. There are many different materials used as electrolyte such as solvent based liquids, polymers or solid state electrolytes. They allow the ion flow inside the battery and restrict the electron flow between electrodes. Separators are basically insulators preventing direct contact between electrodes to avoid short circuit. At the same time, separator should be a good conductor of ions or should soak electrolyte to serve the purpose.

Basic chemical processes occurring at electrodes are shown in Equations 1.1 and 1.2, considering  $\text{LiCoO}_2$  as cathode and graphite as anode material.

Cathode:



Anode:

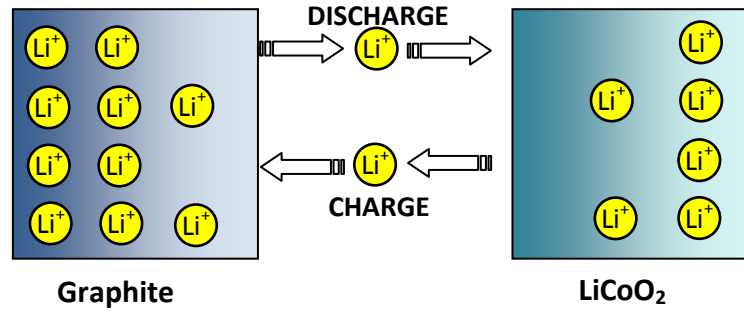


**Figure 1.2:** Li-ion migration during charging and discharging of Li-ion battery with graphite anode and  $\text{LiCoO}_2$  cathode.

**Table 1.1.**  
Lithiated phases and Intercalation capacity of different materials (1).

Materials	Li	C	Si	Sn	Sb	Al	Mg	Bi
Lithiated phase	Li	$\text{LiC}_6$	$\text{Li}_{4.4}\text{Si}$	$\text{Li}_{4.4}\text{Sn}$	$\text{Li}_3\text{Sb}$	$\text{LiAl}$	$\text{Li}_3\text{Mg}$	$\text{Li}_3\text{Bi}$
Theoretical specific capacity (mAh/ g)	3862	372	4200	994	660	993	3350	385
Theoretical charge density (mAh/cm <sup>3</sup> )	2047	837	9786	7246	4422	2681	4355	3765

Researchers are studying many different ways to improve battery performance and one of them is by replacing the currently used anode material by higher capacity material. (Figure 1.3)(2). Because of its advantageous chemical properties, low cost and abundance in nature, carbon has been the first choice anode material in spite of its low reversible capacity which is one of the major limiting factors for higher energy density requirement. Table 1.1 shows the comparison of volumetric and gravimetric capacity of different materials studied recently along with carbon.

The data suggests that Si can be most promising candidate, having maximum gravimetric capacity, low cost and abundance in nature. Major challenges to be faced in replacing carbon with Si as anode material is high volume expansion while alloying with lithium during intercalation process (3). This phenomenon leads to very high mechanical stresses, cracking, pulverizing and eventual failure of anode material. To accommodate this large volume change (300%) and to get better cyclic performance, many different forms of Si are studied, like pure Si powder, Si thin film, Si-active/inactive material composites (see (4) and references therein).

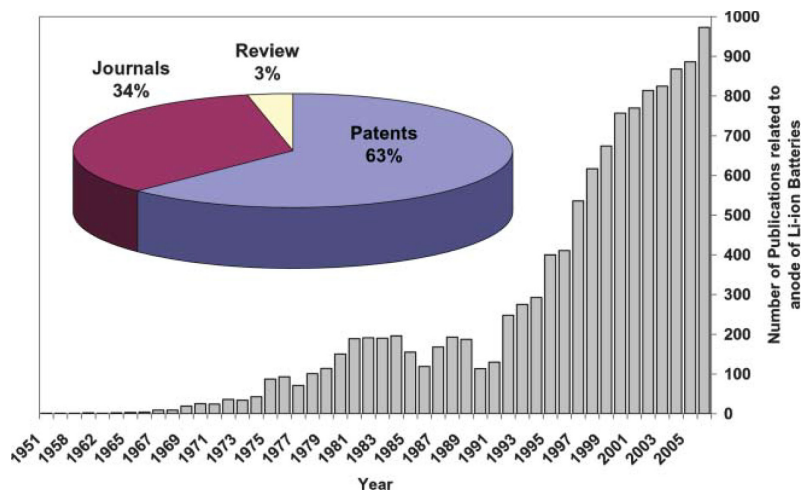


**Figure 1.3:** Publication related to anode materials for Li-ion battery\*.

\*Reprinted by permission from Larcher et al., fig. 1 (1). (See Appendix B for documentation of permission to republish this material)

As mentioned above, failure of anode and consequently reduced life span and performance of the Li-ion batteries is predominantly due to mechanical stresses. To understand the failure mechanisms and structural changes responsible for the performance degradation, sophisticated numerical models are required to replicate the actual physical process occurring during lithiation and delithiation of anode. Many different numerical models suggested recently are based on linear elastic theory and simple geometry (5-9). However the actual phenomena involve very large deformation and the existing models fail to predict failure criteria precisely as well as the exact influence of different mechanisms. The model suggested in present study, being capable of simulating different electrode configurations and complex geometry with large deformation theory and strong coupling between stress and diffusion mechanisms, can be directly validated against experimental results. Thus it can be used as a predictive tool for Li-ion battery anode performance.

In the organization of this thesis, Chapter 2 will discuss various anode configurations and use of the Si as a primary active material. Many different experimental studies are presented showing different phenomena affecting the battery performance. The chapter also contains the literature review of existing numerical models to study the diffusion process showing effect of different parameters. Chapter 3 will present computational frame work with coupled diffusion formulation to study the intercalation induced stresses. The model also includes the cohesive model to simulate the interfacial properties and crack propagation in the anode material along with plasticity effect incorporated in the current model. Results of simulations are presented and discussed in the Chapter 4 and concluded in the Chapter 5 with the recommendations for future work.

# Chapter 2

## Literature Review

Mechanical failure of the electrode material has been identified as the most critical factor for the capacity fade in Li-ion batteries, while trying to improve the energy density by replacing carbonaceous negative electrodes with Silicon or Si-based composite systems. In the alloying process each Si atom can accommodate a maximum of 4.4 Li atoms forming  $\text{Li}_{4.4}\text{Si}$  producing maximum theoretical capacity of 4200 mAh/g (10), which has a volume around 4 times larger than Si atoms (11). Such a large volume expansion is very difficult to accommodate and results in cracking, poor electrical contact and eventual capacity fade. To understand these phenomena, lots of experimental studies have been carried out on alternative systems. Various simulation techniques based on diffusion induced stress and fracture criteria have also been suggested to improve the understanding of the mechanical degradation of the anode material. In this chapter we briefly discuss these experiments and simulations as reported in the literature.

### 2.1 Experimental study

Many different metals and metalloids such as Ti, Si, Sn, Al, Ti and Sb having high theoretical capacity (1,12) are being studied (13-15) as an alternative anode material. In recent times, Si has grabbed a lot of research interest due to its maximum known theoretical capacity among all these candidates and cost effectiveness. In the present study we will focus on the use of Si as an alternative anode material. Use of Si as anode has been studied in various configurations like elemental thin films, nano-architectures (nano-tubes and nano-wires) and as composites.

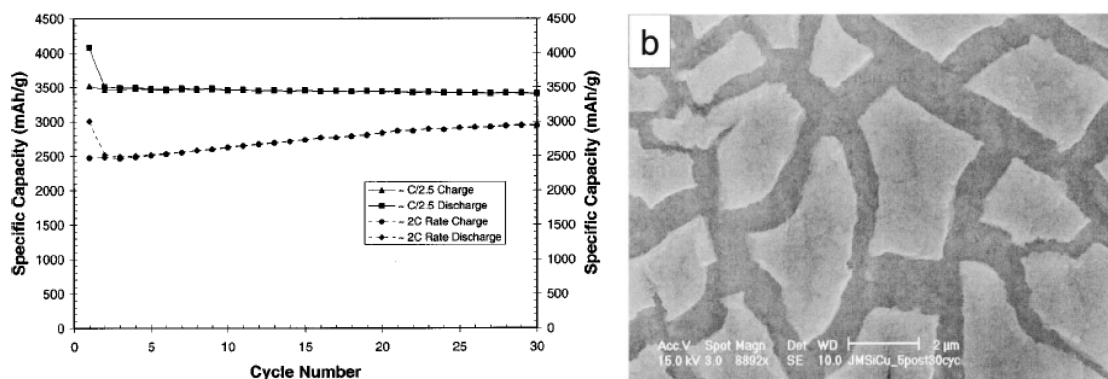


**Figure 2.1:** Si Thin film (a) Specific capacity comparison based on cycling rate (b) SEM Morphology of Si thin film on Cu substrate after 30 cycles\* (16).

### 2.1.1 Silicon Thin films

A number of researchers (16-18) have studied the properties of amorphous silicon thin film of different thicknesses deposited on Cu current collector. Their experiments suggest very high initial capacity  $\sim 3000$  mAh/g up to  $\sim 30$  cycles but the micro structural investigation shows cracking of the film resulting in Si islands attached to Cu substrate (Figure 2.1). In a later study, Maranchi et al. (19) found delamination of those islands and eventual failure of the system after limited number of cycles. During the cycling, formation of Li-Si-Cu phase at the Si-Cu interface was also observed to weaken the interfacial strength.

Many different ways have been suggested to improve the cycle life and reversible capacity of anode materials like using narrow voltage range by upper and lower cut-off voltage restrictions (20-22), or using conductive additives (23) to improve the electronic contact and also the cyclability. But the most effective way has been the reduction of the particle size in the nanometer length scale.

\*Maranchi et al. (16) - Reproduced by permission of The Royal Society of Chemistry (See Appendix C for documentation of permission to republish this material).



Graetz et al. (17) studied the performance of Si thin films with nano-sized crystalline particles and continuous amorphous Si and compared the capacity with bulk Silicon anode, that exhibited improved cyclic performance and better columbic efficiency after few cycles as shown in Figure 2.2.

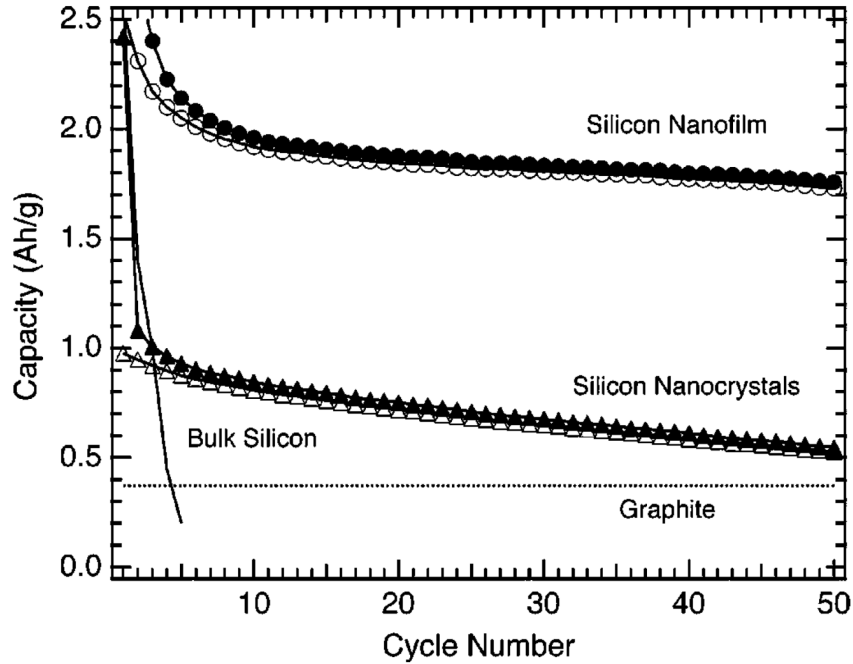


**Figure 2.2:** The gravimetric capacity of the ballistically deposited silicon nanocrystals and the a-silicon nanofilm over 50 cycles, compared with the capacity of graphite ( $\text{LiC}_6$ ) and bulk silicon (17).

Initial high capacity loss in this case shows the evidence of Solid-Electrolyte Interface (SEI) formation which gives irreversible capacity loss by losing Lithium-ions and increased resistance to diffusion process. The a-Si nano film exhibits better performance compared to nano-crystalline anode which can be attributed to elimination of any anisotropic volume expansion occurring in crystalline structure. Many other studies (22,24-26) have also shown the improvement in the cycle life and reduction in the capacity fade due to the capability to accommodate large stress without any crack with nano-sized particles compared to bulk Si-anode material.

### 2.1.2 Silicon Nano-composite

To further enhance the cycle life by reducing the volume change resulting from insertion/extraction of the Li-ions, composite structures comprising of nano-sized Si particles dispersed into active/inactive material matrix that also acts as cohesion between Si particles, is suggested. Many inactive materials TiN (27), TiB<sub>2</sub> (28), SiC (29), TiC (30), etc. has been studied. These materials exhibit much stable reversible capacity for large number of cycles by improving overall mechanical strength of the anode. However these systems exhibits very low specific capacity, probably because of the inactive material hampering ion diffusion process thus not allowing the system to reach its theoretical capacity(4,31) .

A reasonable alternative to this problem can be Si dispersed into active material matrix. Carbon has been a prime contender for the matrix material because of its good conductivity and softness that can absorb the stress generated due to high volume expansion effectively. In some cases it has also been observed to suppress the Solid-Electrolyte Interface to improve the performance. Many different combinations of materials have been used to synthesize the Si/C composite primarily either by pyrolysis or by mechanical milling processes. Yang et al.(26) prepared the composite by thermal pyrolysis at 900°C using polyvinyl chloride, nano-sized silicon and graphite particles. The incorporated anode structure have shown good first cycle efficiency of 85% and much stable cyclic capacity of ~700mAh/g when tested for around 30 cycles. Composition used for the composite was around Si-19.6 wt% Graphite-29.4 wt% and pyrolyzed Carbon-51 wt%. Kim et al. (32) synthesized this composite by High Energy Mechanical Milling(HEMM) prior to pyrolysis from Si and polystyrene (PS). By HEMM process, Si particles were reduced to <50nm size that evenly dispersed into carbon matrix. Composite composition of Si:C=1:2 delivered good capacity retention of ~1.1% loss per cycle with capacity as high as 850 mAh/g. Datta et al. (33) used the similar procedure for composite preparation using silicon, graphite and polyacrylonitrile-based disordered carbon (PAN-C). Here the PAN acts as the diffusion barrier to restrict the formation of inactive SiC which can reduce the overall capacity. As prepared composite

exhibits much more stable cycle capacity of around ~660 mAh/g with negligible capacity reduction for 30 cycles when tested at C/4 rate. Guo (34) used the ball milling process to reduce Si particle size followed by pyrolysis of Si-sucrose and Silicon–polyvinyl alcohol(PVA). The average particle size achieved was 80 nm, and the maximum capacity achieved was 754mAh/g within 20 number of cycles with the composition of 10% Si 90% PVA. Study also suggested that as the Carbon content was reduced, cycle by cycle capacity fade increased, which suggested that Carbon acts to maintain continuous electrical contact among the Si particles and also reduces the electrolyte decomposition at the interface.

Zhang et al. (35) suggested a method of preparing Si/C core-shell composite from Polyacrylonitril (PAN)-coated Si nanoparticles by emulsion polymerization and subsequent heat-treatment under argon atmosphere. Study showed good capacity retention compared to Si anode with increased diffusion coefficient of Li-ions while carbon shell helped restrict Si particle recombined during cycling. Zuo et al. (36) prepared the composite by pyrolyzing the phenol-formaldehyde resin (PFR) mixed with silicon and graphite powders without milling process. The anode material exhibits stable capacity of more than 700 mAh/g. In other studies by Wang et al. (37) and Lee et al. (38) also have shown similar results. In a recent work, Chou et al. (39) achieved much higher reversible capacity with considerably high efficiency using a much simpler technique to prepare Si/graphene composite by simply mixing Si-nano particle with grapheme (Figure 2.3). Anode material composed of ~40 nm Si particle and graphene in same amount shown much higher capacity of 1168 mAh/g for 30 cycles with average columbic efficient of 93%. In another study Hwang et al. (40) have used Si/C composite with inactive elastic polymer microspheres in small amount which reduces the swelling of the anode materials and increases mechanical stability.

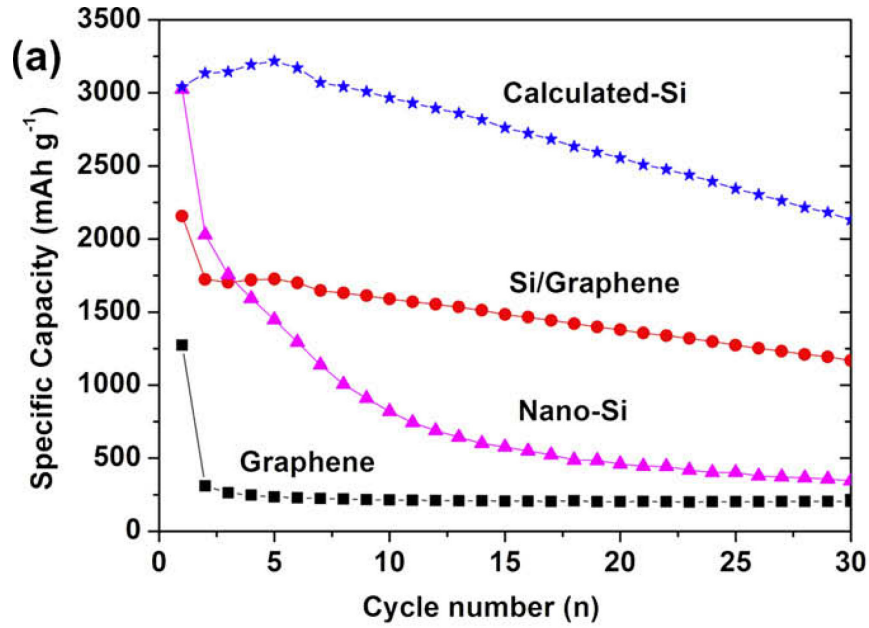


**Figure 2.3:** Specific capacity over the period of 30 cycles for graphene, nanosize Si, Si/graphene composite electrodes, and calculated pure Si contribution from Si/graphene composite (39).

## 2.2 Numerical Models

As we have seen in the previous section, mechanical degradation of the electrode material is one of the severe limiting factors in Li-ion battery capacity fade. A lot of studies have been conducted to improve the energy density of the Li-ion battery using pure Si or Si-composites as an alternative anode material and this problem requires more in-depth understanding of the complex phenomena involved in life time and the failure of the anode. Experimental studies provide only limited information about the failure of the anode structure and a need has arisen to build numerical models that can predict diffusion process, stress evolution and fracture mechanism. A number of studies have suggested analytical models to this end, mainly studying single particle system and simplistic models using small strain formulations loosely coupled with diffusion. Diffusion induced stress and phase transformation effects can be studied in detail with these models, but the

cracking at the interface and the degradation in the electrical contact and resultant effects are difficult to resolve. Also, these models typically demonstrate only single cycle. However, anode degrades over many cycles and thus simulations of more than one cycle is required to understand irreversible changes occurring over cycles of charge and discharge.

### 2.2.1 Numerical studies of single particle electrode for stress evolution

Prussin (41) first analyzed the intercalation induced stress by thermal analogy. Zhang et al. (5) also used the thermal analogy to study the intercalation induced stress in cathode particle ( $\text{LiMn}_2\text{O}_4$ ) with 3D finite element model. Same model can also be used for anode material except for the fact that linear elastic theory appropriate for the small volume changes in  $\text{LiMn}_2\text{O}_4$  (6.5 %) doesn't work well with Si anode having much larger volume expansion (400%). They also displayed how the hydrostatic pressure affects diffusion process with Figure 2.4 showing necessity of considering hydrostatic pressure in the Diffusion equations.

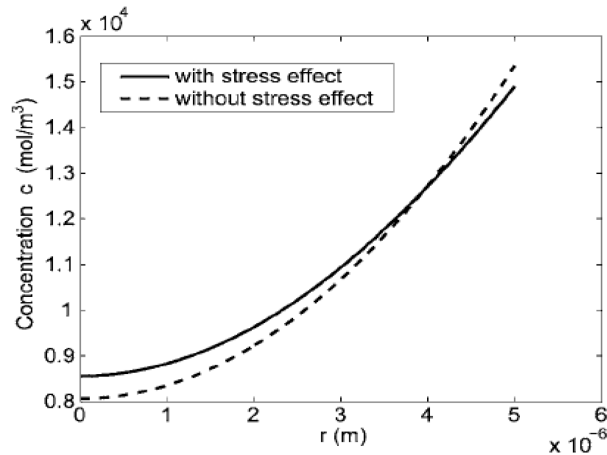


**Figure 2.4:** Comparison of results showing Hydrostatic stress effect (5).

By doing parametric study on particles of different sizes and aspect ratios, result shows better mechanical stability with smaller particle size and larger aspect ratios. In a later study Zhang et al. (6) further developed the model to simulate the cathode material under potentiodynamic condition to study intercalation induced stress along with resistive heating. Their surrogate based model revealed that both the stress and resistive heating increases with increase in particle size and potential sweep rate and decreases with increase in aspect ratio. In a recent study, Park et al. (7) included the effect of phase transformation in the previously used model and suggested that stress due to phase transition are severe than that due to concentration gradient which can cause structural failure at the phase boundary.

Christensen and Newman (42,43) also prepared mathematical models to study the stress generated in a single spherical carbonaceous and Lithium Manganese oxide particle. Their study suggested that electrodes are more vulnerable in the high power applications and smaller particle size increases the fracture strength. Surface of the particle can undergo fracture at the end of the extraction process while core fails at the start of the insertion. Cheng and Verbrugge (8) studied the single spherical particle considering linear elastic theory for diffusion induced stress and strain energy calculation, where simple Fick's law without considering hydrostatic pressure effect has been used to calculate localized concentration. They studied the performance of electrode under galvanostatic and potentiostatic conditions to understand the stress evolution, and displayed the comparison of stress profiles in both conditions to study possible improvement in battery charging strategies improving battery life. Later Cheng and Verbrugge (44) studied the electrode particle under fatigue-stress cycling, and showed that maximum tensile and shear stress occurs in the transition period from charging to discharging and vice versa. They also exhibited importance of faster charge and slower discharge for better mechanical stability. Cheng and Verbrugge (9) also studied the crack initiation by the tensile stress generated during the cycling, comparing with fracture strength of the material. Zhao et al. (45) studied the effect of the particle size and charging rate on the crack propagation by calculation energy release rate of the particle. In a later work Zhao et al. (46) studied the inelastic host (anode) material implementing

elasto-plastic deformation and results suggest better fracture strength for softer materials with smaller size.

### **2.2.2 Numerical studies on Thin film electrodes along with the overall battery performance**

As seen in the previous, section single particle models are the simplistic representation of the electrodes and easy to simulate. However, in actual batteries, electrodes have much more complex structures, and more detailed models are required to understand the failure mechanisms. Chandrasekaran and Fuller (47) studied the Li-ion cell having Si-composite anode, separator and Li foil cathode using porous electrode theory. Suggested 1-D model simulating porosity changes along with the volume changes is solved using commercial software. Their results shows better performance with thicker and porous electrode and suggested optimum values of thickness and porosity, that can be more suitable for the Si electrode to accommodate the high volume expansion associated. They have also introduced the concept of reservoir to accommodate the electrolyte displaced during the process. Danilov et al. (48) also suggest a 1-D mathematical model for all solid state Li-ion battery and compared the voltage profile with experimental data collected with planner thin film solid state Li-ion battery. The model includes various mechanisms such as diffusion of ions in the electrodes and electrolyte and also the charge transfer kinematics at the interface. Their simulation suggests the transfer limitation of solid electrolyte which is considerable in comparison with total overpotential. To understand the failure due to crack propagation in electrode material, Bhandakkar and Gao (49) presented a cohesive model using triangular traction-separation law. The model simulates the initially crack free thin film electrode under the galvanostatic condition for crack nucleation due to diffusion induced stresses. Their analysis suggests the critical thickness below which the crack nucleation can be avoided. Golmon et al. (50) presented multi-scale finite element model to study battery performance, separately at macro- and micro-scale. At macro-scale transport process and deformation was studied for complete battery layer, while at micro-scale single cathode particle is simulated. External mechanical

loads are also considered and effect of the same has been studied. Their results were compared with the previous simulation results and experimental results and shows lower particle-level stress with small size cathode particles. Christensen (51) studied dualfoil Li-ion cell with porous electrode considering effect of pressure diffusion and nonlinear lattice expansion and presented their importance on voltage and stress response during large volume expansions, while Renganathan et al. (52) studied different design parameters of the anode design along with the effect of phase transformation.

### **2.2.3 Models presenting various related phenomena affecting electrode performance**

To understand and improve the overall battery performance, various models are presented concentrating on different phenomena and describing their specific effects. Haftbaradaran et al. (53) studied the surface locking phenomena at the critical value of the product of electrode dimension and charging rate. According to the study, when diffusion process is coupled with internal stresses, at a critical stage concentration at the surface increase drastically due to diffusion locking effect, with high compressive stress generated due to intercalation restricting the diffusion towards the center of the electrode. Haftbaradaran has also suggested the critical values for cylindrical and spherical electrode particle above which surface locking occurs. Deshpande et al. (54) studied the change in the elastic properties of the electrode material with intercalation and deintercalation of the Li-ions. The small strain theory used to simulate the isotropic, homogeneous electrode in cylindrical configuration shows considerable effect on the peak stress considering concentration affected Young's modulus. They also presented the positive effects of Li stiffening during delithiation in the graphite electrode and the Li softening during lithiation in the Si electrode which can help in reducing the cracking failure of the electrode. Shenoy et al. (55) also studied the same phenomena of Li softening specifically in the Si material and compared the behavior of crystalline and amorphous phase during lithiation and showed that amorphous structures are elastically softer than the crystalline electrode. Also the thermal behavior of the cylindrical battery is studied by Jeon and



Baek (56). They presented the mathematical model to study the heat generated by Joule heating and the entropy change, and compared with the experimental data decomposing the effect of different heat sources. Study of different charging and discharging rates on heat generation can be helpful in improving thermal performance and eventually improve the safety aspects.

## **2.3 Research Objective**

As discussed in the previous section, numerical simulation used to predict the complex phenomenon resulting into capacity fade and eventual failure of the electrode material are required in addition to the experimental work. Thus, the objective of the present study is to develop an efficient numerical model to perform simulations on complex electrode configuration and geometries in three dimensions using large deformation theory and strongly coupled diffusion and deformation formulations.

Suggested model will be used to simulate the effect of different materials parameters on crack propagation at the interface between Si-thin film and current collector which can be a major factor for the performance degradation in Li-ion battery due to lose of electrical contact. We will also study the effect of plastic deformation of the current collector with various material properties to quantify its contribution to the failure in failure mechanism. Results of this study will provide accurate effects of various factors contributing to the performance of the Li-ion battery for complex anode configurations. The model will be a significant step towards the complete computational prediction of battery performance under various conditions. As discussed earlier in conjunction with experimental investigations the results of this study will guide designers with feasible design space and provide optimized operating parameters along with better understanding of materials and geometric effect on the overall performance.

# Chapter 3

## Computational Framework

### 3.1. Continuum modeling of diffusion induced expansion

In this section we are going to discuss in detail, the finite element formulation to simulate the Li intercalation induced deformation in the Si based anode materials. Coupled diffusion-mechanical equations in the continuum framework will be illustrated along with the strategy adopted for the solution of these equations in a three dimensional settings.

#### 3.1.1. Kinematic of diffusion induced expansion

Let us consider a body  $\Omega_0$  in its reference configuration having a material point with position vector  $\mathbf{X}$  as shown in Figure 3.1. With the deformation map  $\boldsymbol{\varphi}$ , it can be mapped into current configuration  $\Omega_t$  at time  $t$  as  $\mathbf{x} = \boldsymbol{\varphi}(\mathbf{X}, t)$ . Now as described by Holzapfel (57) for the thermoelastic deformation, multiplicative decomposition can also be used in the similar manner for the intercalation induced deformation as  $\mathbf{F} = \mathbf{F}_e \mathbf{F}_\theta$ . Here the motion  $\boldsymbol{\varphi}(\mathbf{X}, t)$  is decomposed into two successive motions as  $\boldsymbol{\varphi}_e$  and  $\boldsymbol{\varphi}_\theta$  as shown in Figure 3.1. Thus, the deformation gradient  $\mathbf{F}$  and jacobian  $J = \det(\mathbf{F})$  can be described as

$$\mathbf{F} = \frac{\partial \boldsymbol{\varphi}(\mathbf{X}, t)}{\partial \mathbf{X}} = \mathbf{F}_e \mathbf{F}_\theta \text{ and } J = J_e J_\theta > 0, \quad (3.1)$$

Where

$$\begin{aligned}\mathbf{F}_e &= \frac{\partial \varphi_e(\mathbf{X}_\theta, t)}{\partial \mathbf{X}_\theta}, \quad J = \det(\mathbf{F}_e) > 0, \\ \mathbf{F}_\theta &= \frac{\partial \varphi_\theta(\mathbf{X}, t)}{\partial \mathbf{X}}, \quad J_\theta = \det(\mathbf{F}_\theta) > 0.\end{aligned}\tag{3.2}$$

This successive motion introduces an intermediate stress free configuration  $\bar{\Omega}$  solely resulting from intercalation of Li ions. From this definition right Cauchy Green tensor and its elastic counterpart can be defined as

$$\mathbf{C} = \mathbf{F}^T \mathbf{F}, \quad \mathbf{C}_e = \mathbf{F}_e^T \mathbf{F}_e = \mathbf{F}_\theta^{-T} \mathbf{C} \mathbf{F}_\theta^{-1}.\tag{3.3}$$

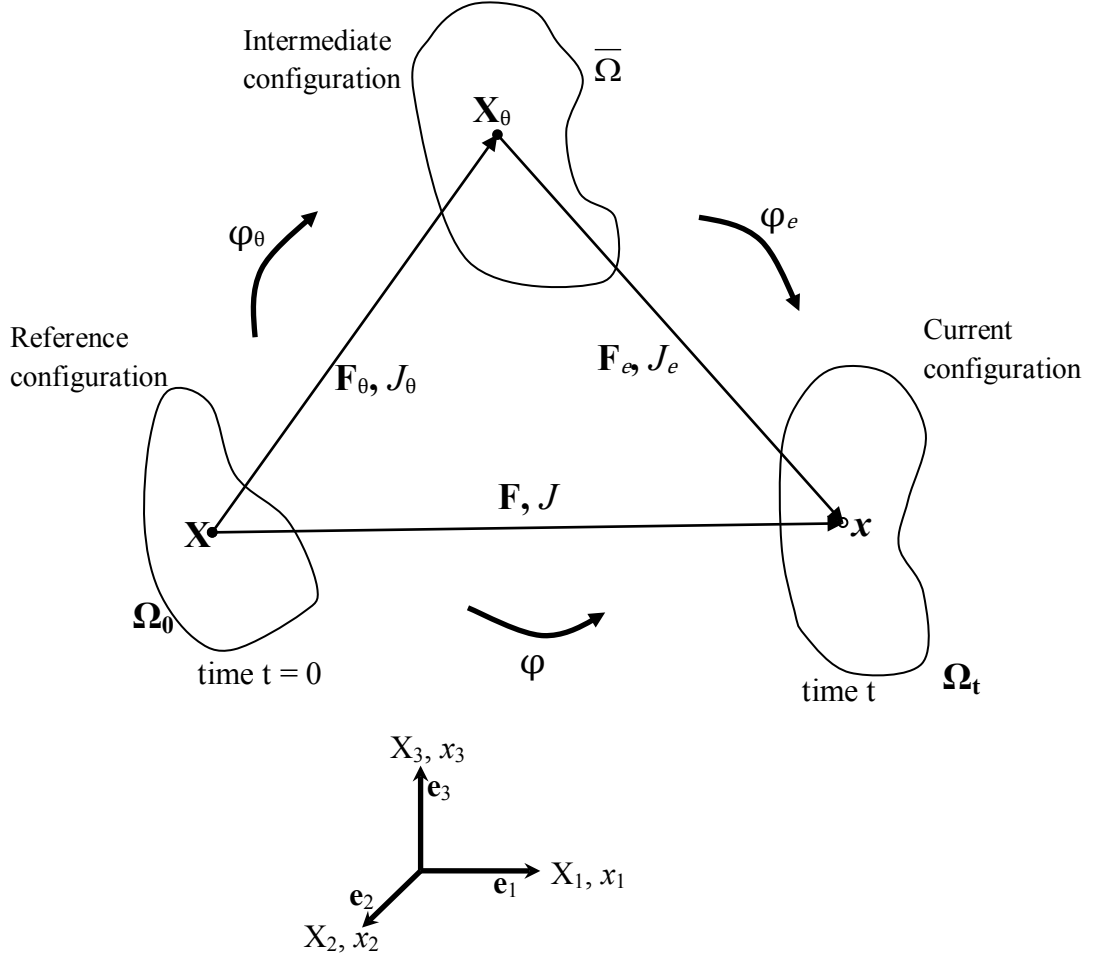


**Figure 3.1:** Graphical representations for multiplicative decomposition of Interpolation induced deformation gradient.

### 3.1.2. Balance equations and constitutive relations

Now, for the isotropic intercalation of the Li-ions we can consider the volume expansion as

$$J_\theta = 1 + \eta c, \quad (3.4)$$

where  $\eta$  is the expansion coefficient, which in this case can be considered as the partial molar volume of the Li-ion in the host material. Also  $c(\mathbf{X}, t)$  is the concentration of the Li-ions in the reference configuration. Thus, the deformation gradient due to intercalation can be presented as

$$\mathbf{F}_\theta = J_\theta^{\frac{1}{3}} \mathbf{I}. \quad (3.5)$$

Herein,  $\mathbf{I}$  is the identity tensor.

Applying conservation of the species' on the Li-ion concentration inside anode material will give us

$$\partial_t c + \nabla_x \cdot \mathbf{J} = 0. \quad (3.6)$$

Here,  $\mathbf{J}$  is the Li-ion flux while  $\nabla_x(\bullet)$  is the divergence of the field in the reference configuration. The initial and the boundary conditions can be described as

$$\begin{aligned} c(\mathbf{X}, t) &= c_0(\mathbf{X}) \text{ on } \partial\Omega_0, \\ \mathbf{J} \cdot \mathbf{N} &= J_0(\mathbf{X}, t) \text{ on } \partial\Omega_0. \end{aligned} \quad (3.7)$$

Where  $J_0$  is the applied Li-ion flux on the material boundary  $\partial\Omega_0$  in the normal direction  $\mathbf{N}$ , which is a transient term. And  $c_0(\mathbf{X})$  is the applied initial concentration at point  $\mathbf{X}(t)$ .

Now, time required for the mechanical equilibrium is much small compared to that required for the ionic diffusion in the solids, so the elastic deformation can be considered as the quasi-static state (5,58). Therefore, the balance of linear momentum can be expressed as

$$\nabla_x \cdot \mathbf{P} = 0, \text{ with } \mathbf{P} = \mathbf{F}\mathbf{S}, \quad (3.8)$$

where  $\mathbf{P}$  and  $\mathbf{S}$  are the first and second Piola-Kirchhoff stress tensor, respectively. The boundary conditions for mechanical equilibrium are given as

$$\begin{aligned} \mathbf{P}\mathbf{N} &= t \text{ on } \partial\Omega_0, \\ u &= u_0 \text{ on } \partial\Omega_0. \end{aligned} \quad (3.9)$$

Where  $t$  is the traction and  $u_0$  is the specific displacement applied at the boundary  $\partial\Omega_0$ . The second Piola-Kirchhoff stress tensor  $\mathbf{S}$  can be derived from a free energy functional applied to the anode material. Here we are considering the free energy functional as

$$\Psi(\mathbf{F}, c) = \Psi_1(\mathbf{F}_e) + \Psi_2(c), \quad (3.10)$$

where  $\Psi_1(\mathbf{F}_e)$  is the elastic part of the free energy which is the function of  $\mathbf{F}_e$ , but from Equation (1) we can see that, it is a function of both the overall deformation gradient  $\mathbf{F}$  and the Li-ion concentration  $c$  (through  $\mathbf{F}_\theta$ ). And the second part  $\Psi_2(c)$  is the chemical energy density of the domain and depends on the ion concentration.

The second Piola-Kirchhoff stress tensor  $\mathbf{S}_e$  and the elastic constitutive moduli  $\mathbf{L}_e$  at the intermediate configuration can be obtained as the first and the second derivative of the free energy functional with respect to right Cauchy-Green deformation tensor as

$$\begin{aligned} \mathbf{S}_e &= 2 \frac{\partial \Psi}{\partial \mathbf{C}_e}, \\ \mathbf{L}_e &= 2 \frac{\partial \mathbf{S}_e}{\partial \mathbf{C}_e} = 4 \frac{\partial^2 \Psi}{\partial \mathbf{C}_e \partial \mathbf{C}_e} \end{aligned} \quad (3.11)$$

Now in the presented model Li-ion intercalation is modeled as the diffusion process with the applied boundary flux  $\mathbf{J}$ , which is considered to be driven by the concentration gradient and the hydrostatic pressure gradient (5,42,50). Thus, the equation of the flux is described as

$$\mathbf{J} = -D\left(\nabla c - \frac{\eta c}{RT}\nabla p\right), \quad (3.12)$$

where  $D$  is the diffusivity of the Li ions in the anode material,  $R$  is the gas constant,  $T$  is the absolute temperature and  $p = \text{tr}(\boldsymbol{\sigma})$  is the hydrostatic pressure, considering  $\boldsymbol{\sigma}$  as the Cauchy stress tensor. Substituting the flux equation into conversation of species Equation (3.6), we get the governing equation for the intercalation of Li-ions in the anode material as

$$\partial_t c = \nabla D\left[\nabla c - \frac{\eta c}{RT}\nabla p\right]. \quad (3.13)$$

### 3.2. Computational modeling of lithium intercalation and stress generation

In this section we will develop a nonlinear finite element framework to simulate the intercalation process of Li-ions in the anode material and the resulting stresses. Our prime focus is to capture the variables such as concentration  $c(\mathbf{X}, t)$  by solving the diffusion equation and the displacement  $\mathbf{u}(\mathbf{X}, t)$  by solving the mechanical equilibrium equation at any material point  $\mathbf{X}$ , at time  $t$ .

### 3.2.1. Operator split technique

To solve the coupled equations presented in previous section we will employ the operator split technique where the system will be solved in two stages. In the first stage the diffusion equation will be solved considering the domain in the mechanical equilibrium.

*Stage I (Intercalation of lithium in anode)*

$$\begin{aligned}\partial_t c &= \nabla D \left[ \nabla c - \frac{\eta c}{RT} \nabla p \right], \\ \dot{u} &= 0,\end{aligned}\tag{3.14}$$

In the second stage mechanical equilibrium equation will be solved at particular time level  $t$  considering the constant concentration at any point  $\mathbf{X}$ .

*Stage II (Mechanical deformation of anode)*

$$\begin{aligned}\nabla \cdot \mathbf{P} &= 0, \\ \dot{c} &= 0.\end{aligned}\tag{3.15}$$

### 3.2.2. Variational form and linearization

The variational form of the governing equation for the Li intercalation, Equation (3.14) can be obtained by Galerkin Weighted Residual Method (GWRM) for any admissible variation  $\delta c$  as

$$\int_{\Omega_0} \delta c \partial_t c \partial \Theta + \int_{\Omega_0} \nabla \delta c D \nabla c \partial \Theta - \int_{\Omega_0} \nabla \delta c \frac{D \eta c}{RT} \nabla p \partial \Theta - \int_{\partial \Omega_0} \delta c J_n \partial \Gamma = 0, \tag{3.16}$$



Furthermore, for any admissible displacement field  $\delta \mathbf{u}$ , the principle of virtual work states that

$$\int_{\Omega_0} \mathbf{S} : \delta \mathbf{E} \partial \Theta - \int_{\partial \Omega_0} \mathbf{t} \cdot \delta \mathbf{u} \partial \Gamma = 0. \quad (3.17)$$

To solve the Equation (3.16) and (3.17) we are using same interpolation functions for concentration field and the displacement field in the domain. The domain  $\Omega_0$  is discretized into  $N_{el}$  elements  $\Omega_0^e$ . Thus the concentration of the Li-ions in the element can be approximated as

$$\tilde{c} = \sum_{i=1}^{n_p} N_c^i \bar{c}_i = \mathbf{N}_c \bar{\mathbf{c}}, \quad (3.18)$$

where  $n_p$  is the number of nodes in the element,  $N_c^i$  and  $\mathbf{N}_c$  are the nodal shape function and the shape function matrix and  $\bar{c}$  is the nodal concentration of Li-ions.

Similarly, the displacement field  $\mathbf{u}$  of the anode within an element is approximated as

$$\tilde{\mathbf{u}} = \sum_{i=1}^{n_p} N_u^i \bar{\mathbf{u}}_i = \mathbf{N}_u \bar{\mathbf{u}}, \quad (3.19)$$

where,  $N_u^i$  and  $\mathbf{N}_u$  are the nodal displacement shape function and shape function matrix.

To discretize the intercalation of Li-ions in time, we dividing the time interval  $t$  into  $n_s$  numbers of subintervals,

$$t = \bigcup_{n=1}^{n_s} [t_n, t_{n+1}]. \quad (3.20)$$

Using the backward Euler scheme we can track the diffusion process of Li-ions in anode between time steps  $[t_n, t_{n+1}]$ . The time derivative of the concentration can be estimated as

$\dot{c} = (c^{n+1} - c^n)/\Delta t$ , where  $\Delta t = (t_{n+1} - t_n)$  is the time step size. And the material gradient of the concentration can be calculated as  $\nabla \tilde{c} = \mathbf{B}_c \tilde{c}$  with  $\mathbf{B}_c = \nabla \mathbf{N}_c$ . So, the residual equations are obtained by substituting the discrete form of concentration of Li-ions as given in Equation (3.18) in variational form of intercalation (3.16) as

$$R_c = \int_{\Omega_0} \delta \tilde{c} \left\{ \frac{\tilde{c}^{n+1} - \tilde{c}^n}{\Delta t} \right\} \partial \Theta + \int_{\Omega_0} \nabla \delta \tilde{c} D \nabla \tilde{c}^{n+1} \partial \Theta - \int_{\Omega_0} \nabla \delta \tilde{c} \frac{D \eta \tilde{c}^{n+1}}{RT} \nabla p^{n+1} \partial \Theta - \int_{\partial \Omega_0} \delta \tilde{c} J_0^{n+1} \partial \Gamma. \quad (3.21)$$

Similarly, substituting discrete form of displacement field (3.19) in principle of virtual work (3.17), the residual equation for the second stage can be expressed as

$$R_u = \int_{\Omega_0} \mathbf{S} : \delta \bar{\mathbf{E}} \partial \Theta - \int_{\partial \Omega_0} \mathbf{t} \cdot \delta \tilde{\mathbf{u}} \partial \Gamma. \quad (3.22)$$

A Newton-Raphson scheme is adopted to solve the residual equations (3.21) and (3.22) through consistent linearization. Linearization of Equation (3.21) at current time step  $t=t_{n+1}$  offers

$$R_c^{k+1} = R_c^k + \frac{\partial R_c}{\partial \tilde{c}^{n+1}} \Delta \tilde{c}_{k+1}^{n+1} \approx 0, \quad (3.23)$$

where,  $(\bullet)_k^n$  denotes the values at time level  $n$  and the Newton Raphson iteration level  $k$ , while  $(\bullet)^n$  and  $(\bullet)^{n+1}$  denote converged values at time level  $n$  and  $n+1$ . Substituting Equation (3.18) in linearized residual equation of intercalation (3.23), it can be rewritten as

$$\mathbf{K}_c \Delta \tilde{c}_{k+1}^{n+1} = \mathbf{R}_c^k \quad (3.24)$$

where, components of  $\mathbf{K}_c$  and  $\mathbf{R}_c^k$  are listed in Appendix A.

Similarly, linearization of residual equation of principle of virtual work (3.22) along with Equation (3.19) gives

$$\mathbf{K}_u \Delta \tilde{\mathbf{u}}_{k+1}^{n+1} = \mathbf{R}_u^k \quad (3.25)$$

where, stiffness matrix  $\mathbf{K}_u$  and load vector  $\mathbf{R}_u^k$  can be written as

$$\begin{aligned} \mathbf{K}_u &= \sum_{e=1}^{n_{el}} \int_{\Omega_o^e} \mathbf{B}_u^T \mathbf{L} \mathbf{B}_u \partial \Theta + \sum_{e=1}^{n_{el}} \int_{\Omega_o^e} \mathbf{B}_0^T \mathbf{S} \mathbf{B}_0 \mathbf{I} \partial \Theta, \\ \mathbf{R}_u &= \sum_{e=1}^{n_{el}} \int_{\partial \Omega_o^e} \mathbf{N}_u^T \mathbf{t} d\Gamma - \sum_{e=1}^{n_{el}} \int_{\Omega_o^e} \mathbf{B}_u^T \mathbf{S} \partial \Theta, \end{aligned} \quad (3.26)$$

where,  $\mathbf{B}_u$  and  $\mathbf{B}_0$  given as

$$\mathbf{B}_u = \text{sym}(\nabla \mathbf{N}_u \mathbf{F}), \quad \text{and } \mathbf{B}_0 = \nabla \mathbf{N}_u, \quad (3.27)$$

respectively. The fourth order tensor  $\mathbf{L}$  represents the lagrangian constitutive moduli as given in Equation (3.11), can be derived directly from the linearization of second Piola Kirchhoff stress  $\mathbf{S}$  with respect to total right Cauchy green tensor  $\mathbf{C}$  for a fixed  $\mathbf{F}_\theta$  as

$$\mathbf{L} = 2 \frac{\partial \mathbf{S}}{\partial \mathbf{C}} \bigg|_{\mathbf{F}_\theta} = [\mathbf{F}_\theta^{-1} \otimes \mathbf{F}_\theta^{-1}] : \mathbf{L}_e : [\mathbf{F}_\theta^{-T} \otimes \mathbf{F}_\theta^{-T}]. \quad (3.28)$$

The above equation can be interpreted as the pull back of the elastic moduli  $\mathbf{L}_e$  onto the reference configuration, where  $\mathbf{L}_e = 2\partial \mathbf{S}_e / \partial \mathbf{C}_e$  are the constitutive moduli of the elastic material as given in Equation (3.11).

### 3.2.3. Solution strategy

An iterative strategy has been adopted to solve the discretized equation for lithium intercalation and mechanical equilibrium of anode at each time step. As mentioned above let  $(\bullet)_k^n$  denotes the values at iteration level  $k$  within time step  $n$ , while  $(\bullet)^n$  denotes converged values at time step  $t_n$ . Our goal is to obtain the converged concentration and displacement field at time step  $n+1$  assuming all the field quantities are known at  $t = t_n$ .

1. Increment time  $t_n$  by  $\Delta t$  i.e., set  $t_{n+1} = t_n + \Delta t$
2. Start iteration with  $k = 0$  and  $(\bullet)_0^n = (\bullet)^n$ 
  - (a) If  $k = 0$ , set  $\bar{\mathbf{u}}_0^{n+1} = \bar{\mathbf{u}}^n$  and find  $\bar{\mathbf{c}}_{k+1}^{n+1}$  from Equation (3.24)
  - (b) Compute  $\bar{\mathbf{u}}_{k+1}^{n+1}$  from Equation (3.25) using  $\bar{\mathbf{c}}_{k+1}^{n+1}$
  - (c) Check convergence criteria

$$\text{If } \frac{\|\bar{\mathbf{u}}_{k+1}^{n+1} - \bar{\mathbf{u}}_k^{n+1}\|_2}{\|\bar{\mathbf{u}}_0^{n+1}\|_2} \leq \epsilon_{tol}^u \quad \text{and} \quad \frac{\|\bar{\mathbf{c}}_{k+1}^{n+1} - \bar{\mathbf{c}}_k^{n+1}\|_2}{\|\bar{\mathbf{c}}_0^{n+1}\|_2} \leq \epsilon_{tol}^c$$

Then repeat step 1 else set  $k = k+1$  and go to step 2(a)

## 3.3. Modeling of plastic deformation in current collector

As suggested by Maranchi (19), because of the large amount of the volume expansion in the Si during lithiation, plastic deformation of the underlying current collector is unavoidable and can have a major contribution in the failure of the anode structure. To resolve such deformation mechanism we have proposed a finite deformation based plasticity formulation for the current collector. Here multiplicative decomposition of the total deformation gradient is considered as

$$\mathbf{F} = \mathbf{F}_e \mathbf{F}_p, \quad (3.29)$$

where  $\mathbf{F}_e$  and  $\mathbf{F}_p$  are the elastic and plastic part of the total deformation gradient respectively, considering mapping of reference configuration ( $\Omega_0$ ) to intermediate configuration ( $\bar{\Omega}$ ) by  $\mathbf{F}_p$  and mapping of intermediate configuration ( $\bar{\Omega}$ ) to spatial configuration ( $\Omega$ ) with  $\mathbf{F}_e$ . The velocity gradient in the spatial configuration from the above multiplicative decomposition can be obtained as

$$l = \dot{\mathbf{F}}\mathbf{F}^{-1} = \dot{\mathbf{F}}\mathbf{F}_e^{-1} + \mathbf{F}_e \dot{\mathbf{F}}_p \mathbf{F}_p^{-1} \mathbf{F}_e^{-1}. \quad (3.30)$$

Also the pull back of the spatial velocity gradient to the intermediate configuration can be defined as

$$\mathbf{L} = \mathbf{F}_e^{-1} l \mathbf{F}_e = \dot{\mathbf{F}}_e \mathbf{F}_e^{-1} + \dot{\mathbf{F}}_p \mathbf{F}_p^{-1} = \mathbf{L}_e + \mathbf{L}_p, \quad (3.31)$$

where  $\mathbf{L}_e$  and  $\mathbf{L}_p$  are the elastic and plastic part of the velocity gradient respectively and can be defined as  $\mathbf{L}_e = \dot{\mathbf{F}}_e \mathbf{F}_e^{-1}$  and  $\mathbf{L}_p = \dot{\mathbf{F}}_p \mathbf{F}_p^{-1}$ . In this study we are assuming the flow rule in terms of the plastic part of the velocity gradient as

$$\mathbf{L}_p = \dot{\mathbf{F}}_p \mathbf{F}_p^{-1} = \dot{\lambda} \mathbf{N}_p, \text{ where } \mathbf{N}_p = \frac{\partial f}{\partial \mathbf{M}_e} \quad (3.32)$$

where  $\dot{\lambda}$  is a plastic strain rate constant and  $\mathbf{N}_p$  is a vector normal to the yield surface which defines the direction of the plastic flow. Also the Mandel stress tensor  $\mathbf{M}_e$  and yield function  $f$  are defined in Equation 3.33 and 3.34 respectively.

$$\mathbf{M}_e = \mathbf{C}_e \mathbf{S}_e, \quad (3.33)$$

where  $\mathbf{C}_e$  and  $\mathbf{S}_e$  are the elastic part of right Cauchy-Green deformation tensor and second Piola-Kirchhoff stress tensor respectively. The yield function with linear hardening considered in this study as

$$f(\mathbf{M}_e, \bar{\varepsilon}_p) = \sqrt{\frac{3}{2} \mathbf{M}_e^d : \mathbf{M}_e^d} - [\sigma_0 + H \bar{\varepsilon}_p] = 0, \quad (3.34)$$

where  $\mathbf{M}_e^d$  is the deviatoric part of the Mandel stress tensor,  $\sigma_0$  is the yield stress and  $H$  is the hardening parameter. Also the accumulated plastic strain  $\bar{\varepsilon}_p$  is defined as

$$\bar{\varepsilon}_p = \sqrt{\frac{3}{2}[\mathbf{E}_p : \mathbf{E}_p]} = \int \dot{\lambda} dt \text{ where } \dot{\bar{\varepsilon}}_p = \dot{\lambda} \quad (3.35)$$

where  $\mathbf{E}_p$  is the plastic part of the Lagrangian strain tensor. Here according to the Kuhn-Tucker condition, loading-unloading can be defined as  $\dot{\lambda} \geq 0, f(M_e, \bar{\varepsilon}_p) \leq 0$  and  $\dot{\lambda} f(M_e, \bar{\varepsilon}_p) = 0$ . Also the consistency condition  $\dot{f}(M_e, \bar{\varepsilon}_p) = 0$  has to be satisfied.

### 3.4. Cohesive zone model for crack propagation

Electro-chemical degradation of the electrode material is often characterized by the delamination of the thin film from the substrate. As the work of Maranchi et al. (19) suggests, islands formed in the Si-thin film after the first cycle. This work also shows eventual delamination from the substrate after a specific number of cycles. Thus, loss of the electrical contact between active material and current collector reduces the reversible capacity and affects the integrity of the anode structure. To understand the effect of the crack propagating through the interface it is important to introduce the cohesive zone modeling which can simulate the failure of the binder material at the interface.

For the cohesive zone modeling we will follow the numerical frame work suggested by Ortiz and pandolfi (59), and also use the failure criteria and the traction separation law they presented. To understand the behavior of the cohesive zone first let us consider a body in its initial condition as  $B_0 \subset R^3$ . The motion of the body is described by  $\varphi: B_0 \rightarrow R^3$  under the body forces of  $\rho_0 b$  and boundary traction  $\mathbf{t}$ . The body is divided into two parts by the cohesive zone  $S_0$  as  $B_0^+$  and  $B_0^-$  respectively as shown in Figure 3.2.

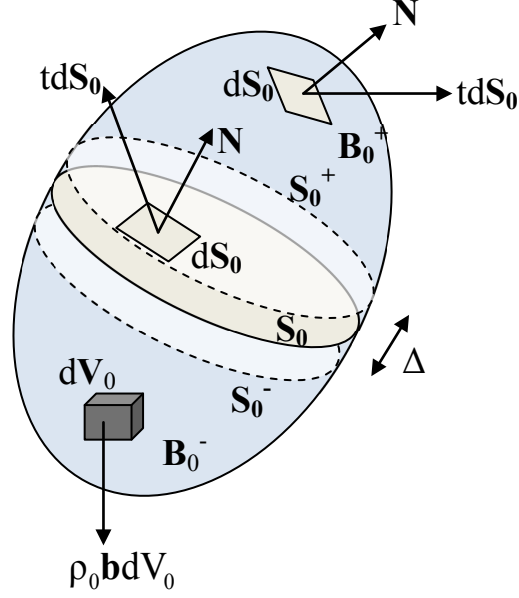


**Figure 3.2:** Representative volume with cohesive surface.

Principle of virtual work can be applied to such body as,

$$\int_{B_0} [\rho_0 \mathbf{b} \cdot \boldsymbol{\eta} - \mathbf{P} \nabla_0 \boldsymbol{\eta}] dV_0 - \int_{S_0} \mathbf{T} \cdot \Delta dS_0 + \int_{\partial B_0^+} \mathbf{t} \cdot \boldsymbol{\eta} dS_0 = 0 \quad (3.36)$$

Where  $\boldsymbol{\eta}$  is an arbitrary virtual displacement,  $\nabla_0$  is the material gradient,  $\mathbf{T}$  is the cohesive traction and  $\Delta$  is the displacement jump. Here we can see that cohesive surface has added an extra term in the expression. For the particular problem we can assume the free energy density over the area  $S_0$  as

$$\phi = \phi(\Delta_n, \Delta_t, q), \quad (3.37)$$

where  $q$  is the variable describing the amount of decohesion. The cohesive law considered in this model, can be presented as Equation 3.38.

$$\mathbf{T} = \frac{\partial \phi}{\partial \Delta} \quad (3.38)$$

Now, the cohesive law we are going to use here is an irreversible relation between traction and separation, with internal variable considered as maximum effective

separation ( $\Delta_{max}$ ). For the loading condition ( $\Delta = \Delta_{max}$ ) we are using exponential relation Equation. (3.39) suggested by Smith and Ferrante (60), while for the unloading ( $\Delta < \Delta_{max}$ ) condition towards origin we are following Camacho and Ortiz (61) Equation (3.40). This relation is also explained in the Figure 3.3.

$$t = e\sigma_c \frac{\Delta}{\Delta_c} e^{-\Delta/\Delta_c} \text{ for } \Delta = \Delta_{max} \quad (3.39)$$

$$t = \frac{t_{max}}{\Delta_{max}} \Delta \text{ for } \Delta < \Delta_{max} \quad (3.40)$$

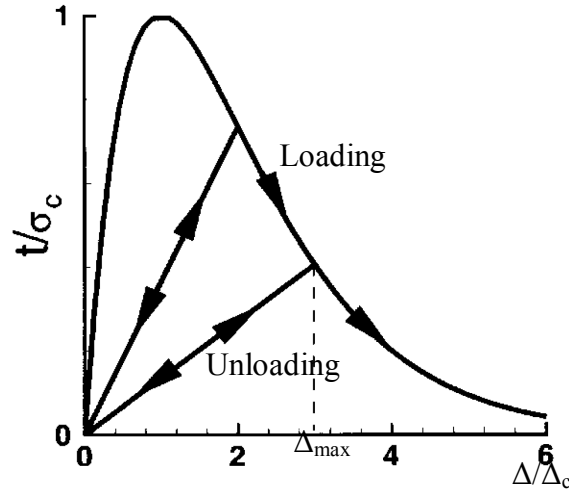


**Figure 3.3:** Loading- unloading path for traction-separation law.



### 3.4.1. Finite Element Implementation

Cohesive volumetric finite element (CVFE) scheme, described in this work using the principle of virtual work given in Equation (3.41) (62) is a finite element implementation of the cohesive model presented in previous section by Equation (3.39) and (3.40).

$$\int_{\Omega} \mathbf{S} : \delta \mathbf{E} d\Omega - \int_{\Gamma_{ex}} \mathbf{T}_{ex} \cdot \delta \mathbf{u} d\Gamma_{ex} - \int_{\Gamma_c} \mathbf{T}_n \delta \Delta_n d\Gamma_c = 0 \quad (3.41)$$

Where  $\mathbf{S}$  and  $\mathbf{E}$  are the stress and the strain tensor respectively,  $\mathbf{T}_{ex}$  is the external traction applied on the body and vector  $\mathbf{u}$  represents the displacement. In the above expression the virtual work done by the cohesive traction  $\mathbf{T}_n$  for the separation  $\Delta_n$  is represented by the last term. The first term representing the internal virtual work depends on the volumetric elements, which influences the value of stress  $\mathbf{S}$  and the virtual strain  $\delta \mathbf{E}$ . Cohesive stiffness matrix  $\mathbf{K}_{coh}$  for the cohesive elements in this case can be derived from the cohesive part of the above virtual work expression as below.

$$\mathbf{K}_{coh} = \int_{\Gamma_c} \mathbf{N}^T \frac{\partial \mathbf{T}_n}{\partial \Delta_n} \mathbf{N} d\Gamma_c + \frac{1}{2} \int_{\Gamma_c} \frac{\partial \mathbf{T}_n}{\partial n} \frac{\partial n}{\partial \bar{x}} \mathbf{N} d\Gamma_c \quad (3.42)$$

Where  $n$  is the cohesive surface normal direction and  $\bar{x}$  is the mid surface coordinate tensor. Cohesive traction  $\mathbf{T}_n$  can be described as,

$$\mathbf{T}_n = \frac{t}{\Delta} \left[ \beta^2 \Delta_n + (1 - \beta^2) (\Delta_n \cdot \mathbf{n}) \mathbf{n} \right], \quad (3.43)$$

where  $\beta$  assigns different weight to the normal and the sliding opening displacement, while  $t$  and  $\Delta$  are the values of the effective cohesive traction and effective opening displacement.

## 3.5. Verification of the Numerical Framework

Different components of the model presented in the previous section are validated against number theoretical results. We are presenting these verification problems in the current section.

### 3.5.1. Diffusion in the semi-infinite region

For the theoretical verification of presented transient diffusion model, we will be solving simple diffusion problems in semi-infinite domain (Figure. 3.4). In these cases, we will neglect the hydrostatic pressure effect which simplifies the earlier proposed diffusion Equation (3.13) as below.

$$\partial_t c = D \nabla^2 c \quad (3.44)$$

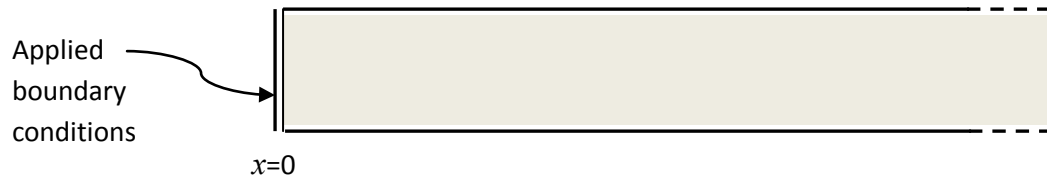


**Figure 3.4:** Semi infinite bar with applied boundary conditions at  $x = 0$ .

For the given boundary conditions we will calculate concentration  $C(x, t)$  at different time steps throughout the domain and compare the results with the analytical results.

Case 1: Fixed concentration at one end of semi-infinite domain with no outward flux from any surfaces.

Boundary conditions:

$$\begin{cases} C(x, t) = C_0 & x = 0, \\ C(x, 0) = 0 & \text{at } x > 0. \end{cases}$$

Analytical solution for this problem can be given as(63),

$$C(x, t) = C_0 \left( \operatorname{erfc} \left( \frac{x}{2\sqrt{Dt}} \right) \right) \quad (3.45)$$

Case 2: Fixed applied flux  $J_0$  at  $x = 0$  with no outward flux from any other surfaces.

Boundary conditions:

$$\begin{cases} J(x, t) = J_0 & x = 0, \\ C(x, 0) = 0 & \text{at } x > 0. \end{cases}$$

Concentration profile in the body can be presented as equation below. (64)

$$C(x, t) = - \left( \frac{J_0}{\sqrt{D}} \right) \left( 2\sqrt{\frac{t}{\pi}} e^{(-x^2/4Dt)} - \frac{x}{\sqrt{D}} \operatorname{erfc} \left( \frac{x}{2\sqrt{Dt}} \right) \right) \quad (3.46)$$

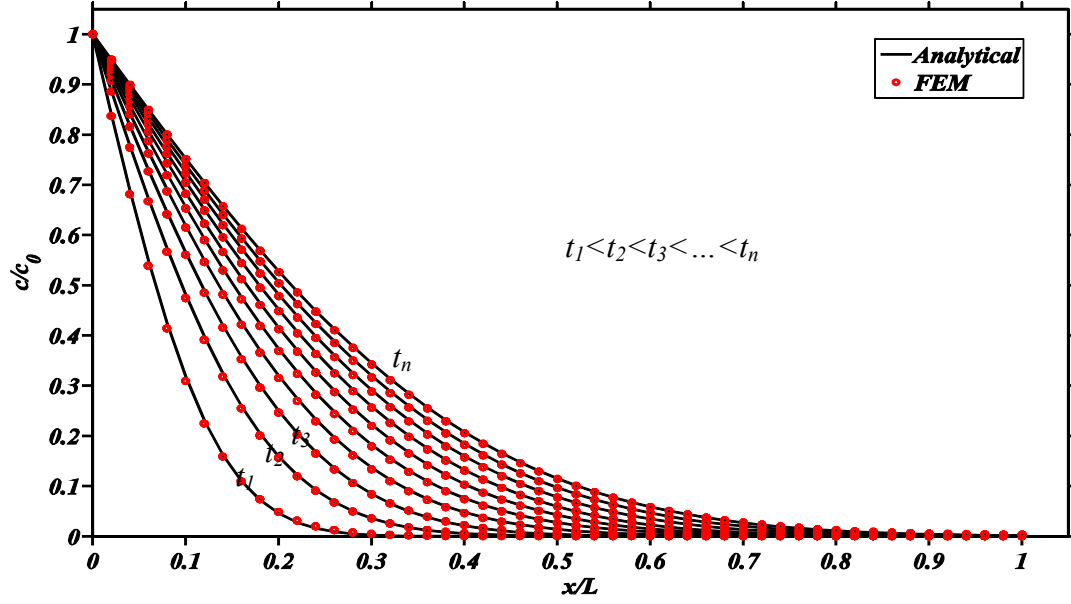


**Figure 3.5:** Verification of case 1 with fixed Concentration ( $C_0$ ) at  $x = 0$ .

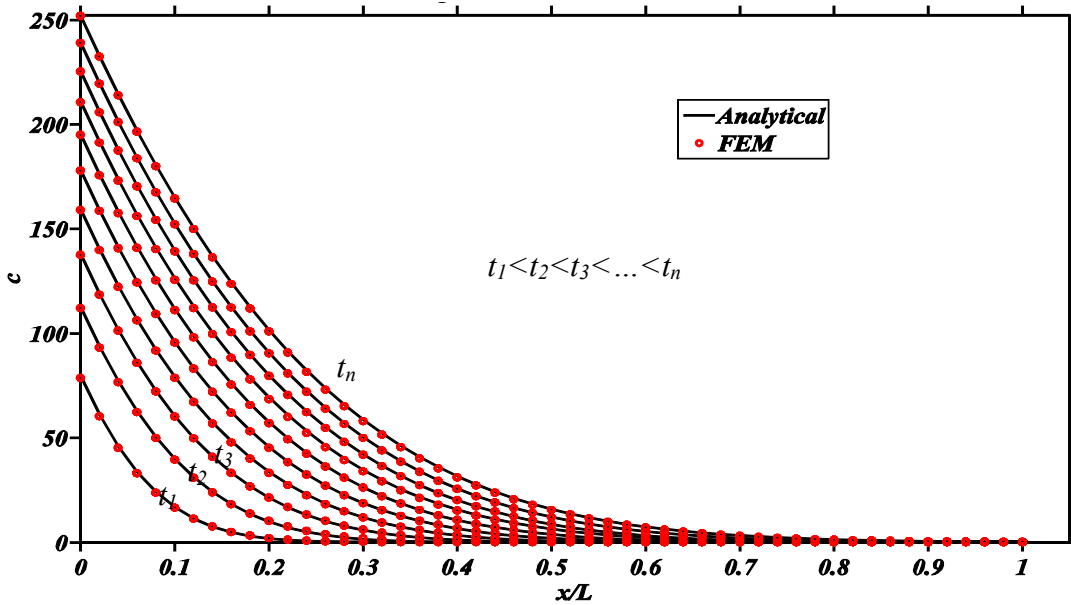


**Figure 3.6:** Verification of case 2 with fixed flux ( $J_0$ ) at  $x = 0$ .

To simulate these problems, a long bar with length  $L = 10$  cm and width and thickness of 1 cm is used as a domain. Also the length of bar is much longer than the Diffusion length which is  $L_D = 2\sqrt{Dt}$ , so that the concentration does not reach to the other end of the bar and domain can be considered as a semi-infinite body. Domain is discretized with

hexahedron elements. As the equation is solved implicitly, formulation is unconditionally stable, and time step size is not restricted to a specific value. It can be observed from Figure 3.5 and 3.6 that simulation results coincide exactly with the analytical curves. Thus, the proposed solution method can be used as a predictive model for the diffusion of Li-ions in the Si anode material.

### 3.5.2. Bending of Bimetallic strip under thermal loading

To verify the formulation for the diffusion induced deformation in the electrode, we will be inspecting the simulation results for the bimetallic strip deformation at an elevated temperature. As suggested by Chang et al. (9) and Renganathan et al. (52), concentration variable  $C(x, t)$  in the diffusion Equation (3.13) is analogous to the temperature in the thermal diffusion. Thus, the proposed ion-diffusion problem can be transformed into the thermal problem for buckling of the bimetallic strip under thermal expansion.

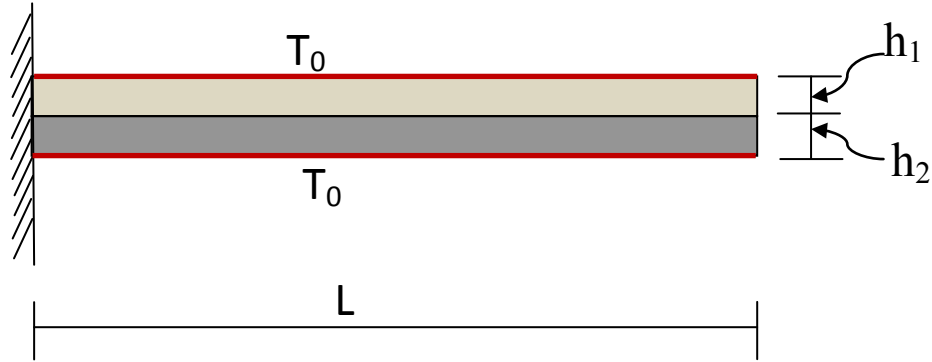


**Figure 3.7:** Bimetallic strip with applied temperature at top and bottom surfaces.

**Table 3.1**  
Material variables and dimensions used for the simulation.

	E (GPa)	$\nu$	L (cm)	h (cm)	$\alpha$ (m/m°C)	T <sub>0</sub> (°C)
Material - 1	112	0.33	50	0.5	14e-6	400
Material - 2	112	0.33	50	0.5	2 e-6	400

As shown in Figure 3.7 we will be considering a fixed beam with two different materials having same thicknesses and length L, with applied constant temperature T<sub>0</sub> at top and bottom surfaces. Diffusion process is simulated till we get homogeneous temperature distribution throughout the body. The deformation of the free end will be measured and compared with the analytical study suggested by Boley (65) for bimetallic strip deflection, for materials having same mechanical properties but different thermal expansions. Equation for the deflection at x = L can be presented as,

$$\Delta = \frac{6L^2(\alpha_2 - \alpha_1)T}{16h}. \quad (3.47)$$

All the variables and the dimensions used for the simulation are as given in table 3.1.

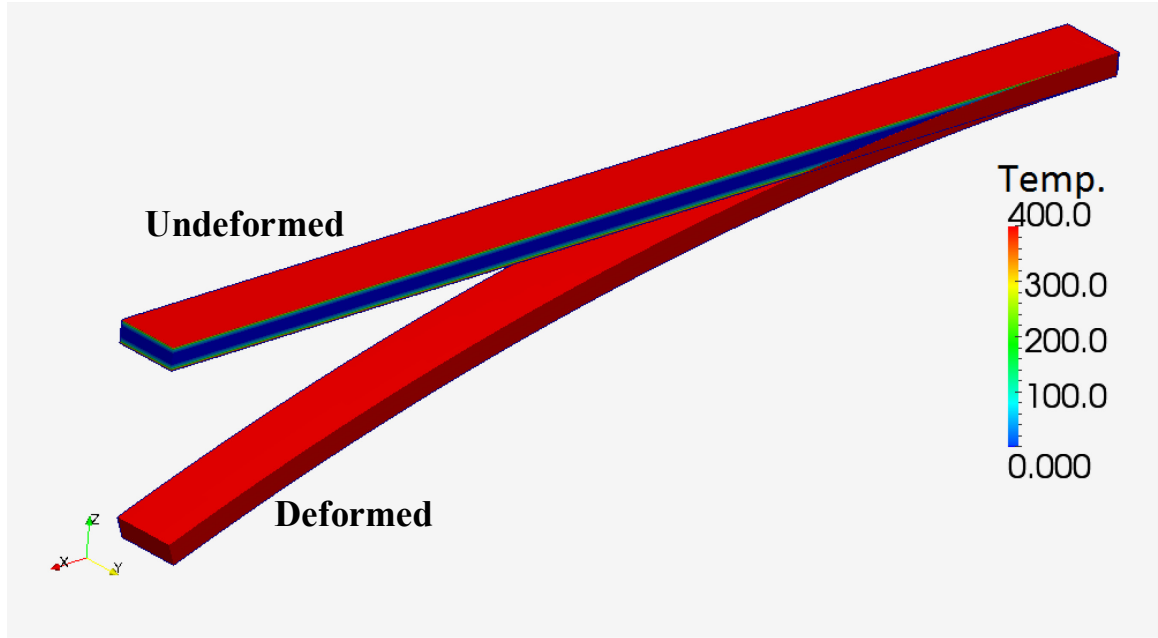


**Figure 3.8:** Bimetallic strip comparison of deformed and undeformed configuration.

The problem is simulated by solving the transient diffusion equation coupled with the static mechanical problem implicitly. As presented in table 3.2 simulation results are a close match with the analytically calculated deflection. Thus, the proposed formulation and the solution method can be used for the prediction of the diffusion induced stress in the anode material.

**Table 3.2**  
Comparison of Simulation results with analytical for deflection at the free end of bimetallic strip.

	Analytical	Simulation	Relative error
Deflection	9 cm	8.867 cm	3.5 %

# Chapter 4

## Results and Discussion

The numerical model presented in Chapter 3 has been used to simulate the anode structure through lithiation/delithiation cycles and the chemo-mechanical response of the domain is studied. In this chapter we will be discussing the results of these simulations on anode structure comprising Si thin film, current collector and binding material at the interface. As mentioned earlier, after the first cycle of charging and discharging, Si film undergoes fracture and forms islands attached to the current collector (16). Thus, in this study we will simulate volume expansion of a single Si island along with the elastoplastic deformation of the substrate attached to it and crack propagation at the interface. Effect of various material parameters of the current collector and the interface will be studied to understand the failure mechanism and propose better and stable anode structure utilizing the Si thin film. Detailed problem description is given in the following section along with the material and simulation parameters used.

### 4.1. Problem description

To study the anode structure, we have considered a three-dimensional domain as shown in the Figure 4.1, where bottom substrate represents the current collector and the top island represents the Si thin film having a cohesive layer in between. Si thin film thickness is considered as 250 nm with  $1\text{ }\mu\text{m} \times 1\text{ }\mu\text{m}$  sized island, and 3 times larger dimensions are considered for the substrate to sustain the volume expansion of the island having rigid support at the bottom surface. As we are



considering galvanostatic charging and discharging, constant Li-ion flux is applied through the top surface of the Si-island as shown in Figure 4.1. Also required input parameters for the simulation are listed in the Table 4.1

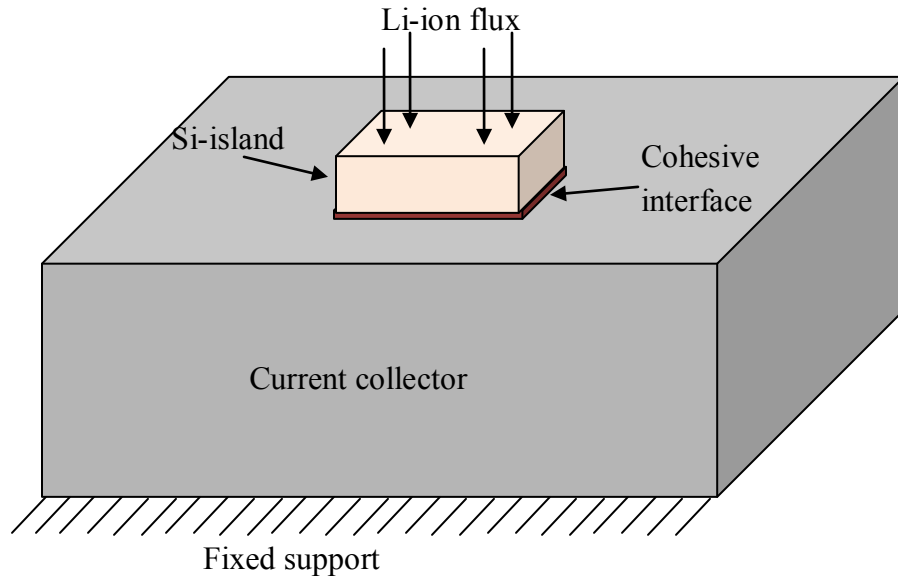


**Figure 4.1:** Si-island subjected to Li-ion flux, attached to current collector. Structure has a fixed support at the bottom.

**Table 4.1**  
Input data required for the Numerical simulation

<b>Silicon-island Material parameters</b>	<b>Substrate Material Parameters</b>	<b>Cohesive parameters</b>	<b>Simulation parameters</b>
$E$ - Young's modulus	$E$ - Young's modulus	$\sigma_c$ – Critical stress	Charging rate
$\nu$ - Poisson's ratio	$\nu$ - Poisson's ratio	$\Delta_c$ – Critical separation	Number of steps per cycle
$D$ - Diffusion coefficient	$\sigma_y$ – Yield stress		Li-ion flux
$\eta$ - Expansion coefficient	$H$ - Hardening Parameter		

In this numerical study material data for the Si-island given in Table 4.2 are used for all the simulation results presented here.

As we can see the domain is symmetric along the two of the coordinate axis. Thus taking the advantage of this symmetry we are considering the 1/4<sup>th</sup> of the domain presented in Figure 4.1 for computational saving as shown in Figure 4.2. Appropriate symmetric boundary conditions are applied on the surfaces of the symmetry.

**Table 4.2**  
Material data for Si thin film used in the simulations.

<b>Parameter</b>	<b>Symbol</b>	<b>Value</b>
Young's Modulus	$E$	80 GPa
Poisson's ratio	$\nu$	0.28
Diffusion Coefficient	$D$	1e-16 m <sup>2</sup> /s
Expansion Coefficient	$\eta$	9e-6 m <sup>3</sup> /mol

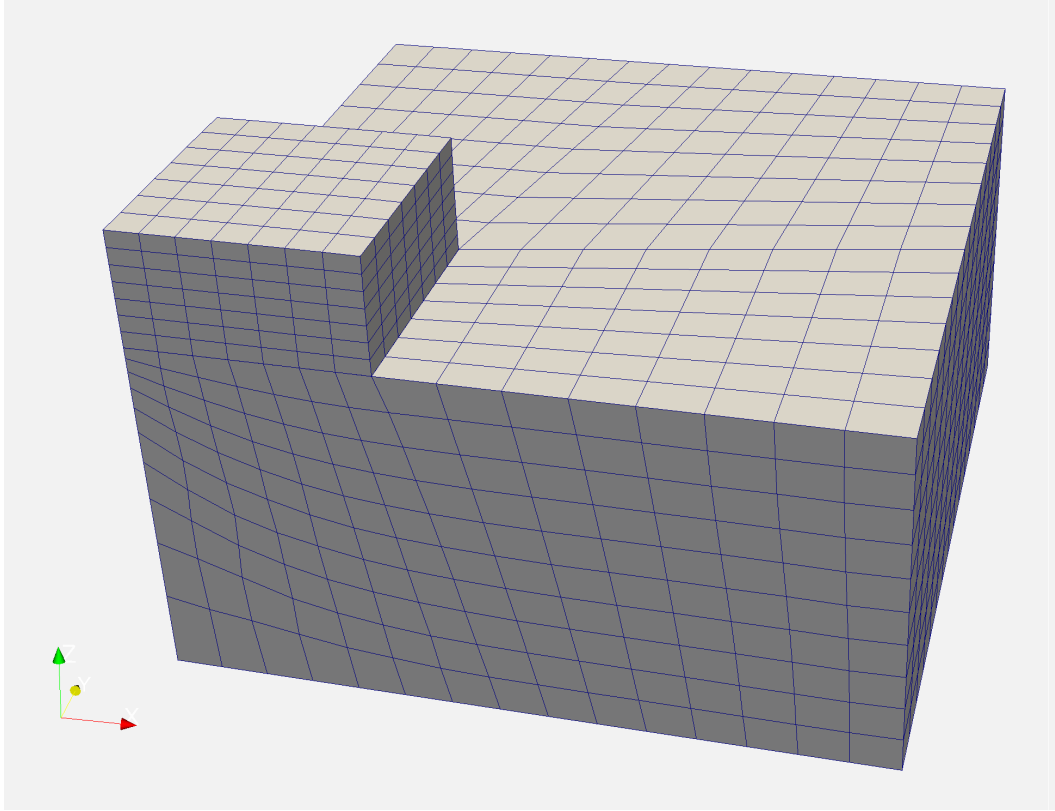


**Figure 4.2:** Symmetric portion of the domain considered for the simulation.

## 4.2. Li-ion intercalation process

To simulate the Li-ion diffusing from electrolyte at galvanostatic condition, we are applying the constant Li-ion flux at the top surface till the surface concentration reaches the maximum material capacity and applied flux direction will be inverted in the delithiation cycle. As a result concentration profile achieved for the diffusion process during lithiation and delithiation cycles are shown in the Figure 4.3 and Figure 4.4 respectively.

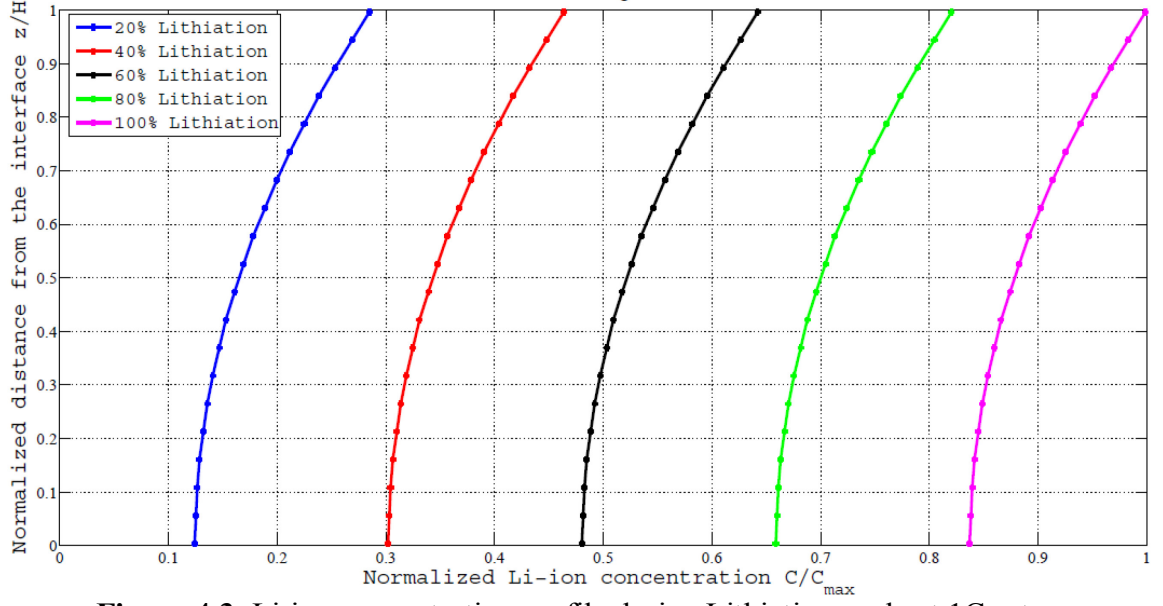


**Figure 4.3:** Li-ion concentration profile during Lithiation cycle at 1C-rate.

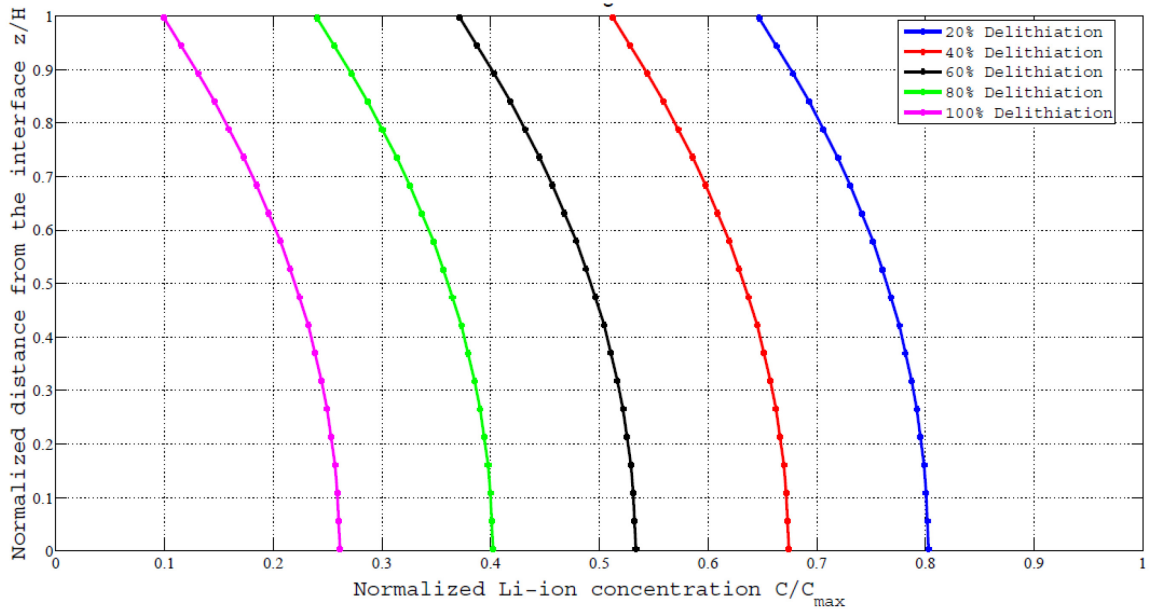


**Figure 4.4:** Li-ion concentration profile during Delithiation cycle at 1C-rate.

Because of the Li-ion intercalation process, we are getting large volume expansion in the island, here the geometric deformation not only depends on the partial molar volume of the intercalated Li-ions in the  $\text{Li}_x\text{Si}$  phase, but also affected by the interface and substrate

material properties as it is restricting the expansion. Comparison of deformed and undeformed conditions of Si-island at the end of lithiation and delithiation cycle is presented in the Figure 4.5 and Figure 4.6. Permanent plastic deformation can be seen in the deformed conditions at the end of lithiation cycle while onset of the fracture occurs at the edge at the end of delithiation.

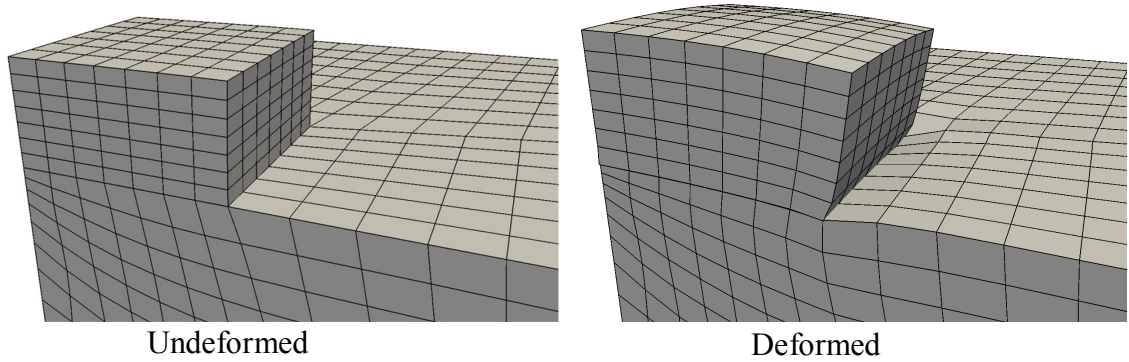


**Figure 4.5:** Comparison of deformed and undeformed conditions at the end of the lithiation cycle.

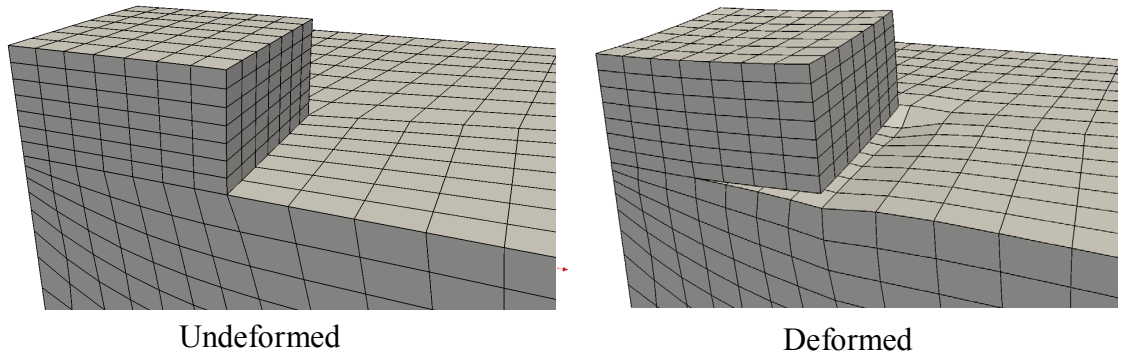


**Figure 4.6:** Comparison of deformed and undeformed conditions at the end of the delithiation cycle.

### 4.3. Effect of interfacial material properties on crack initiation

In this section we are presenting a parametric study on the electrode configuration described above with various interface material prosperities, keeping the material properties of the substrate as well as Si-island constant. For this study we are considering elastic modulus of the substrate  $E = 100$  GPa and Poisson's ratio  $\nu = 0.36$ , and we are neglecting the plasticity effect in this case. We are considering the cohesive toughness ( $G_c$ ) in the range of  $10 \text{ J/m}^2$  to  $30 \text{ J/m}^2$  while cohesive strength ( $\sigma_c$ ) is varying from 500 MPa to 2 GPa. We are simulating only one lithiation/delithiation cycle because in the absence of the plasticity there will not be any change in diffusion and deformation processes in the subsequent cycles.

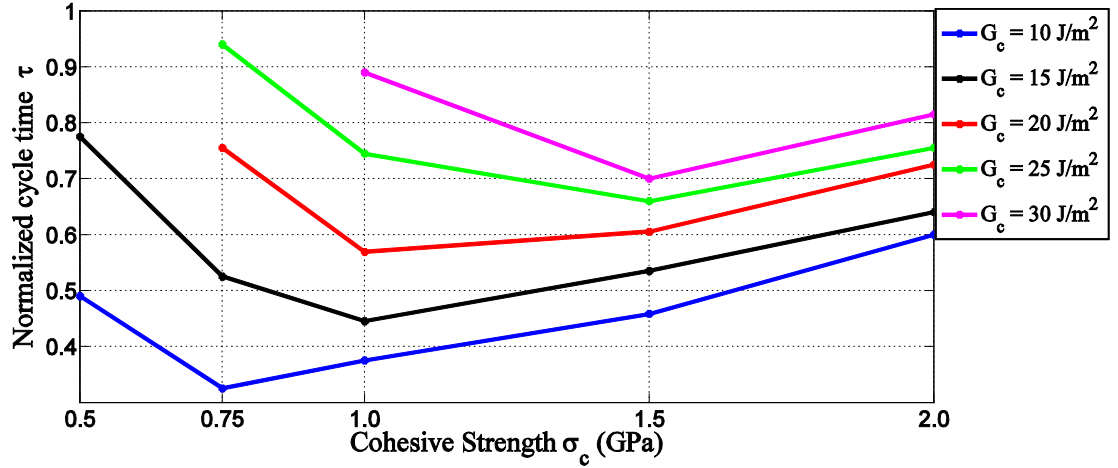


**Figure 4.7:** Time of crack initiation for various cohesive toughness ( $G_c$ ) and cohesive strength ( $\sigma_c$ ) considering constant elastic modulus of substrate  $E=100$  GPa.

In Figure 4.7 normalized lithiation cycle time ( $\tau$ ) of crack initiation at the cohesive interface between Si-island and the substrate is presented against the cohesive strength of the binding material for different values of  $G_c$ . From the data we can clearly see that the crack propagation is delayed with higher value of  $G_c$ . In these numerical simulations

failure takes place only during charging cycle and crack starts from the center of the island. Major reason for the crack initiation is buckling effect in the island as shown in Figure 4.8. During lithiation  $\sigma_c$  affects the crack propagation in two different ways; higher  $\sigma_c$  resists the cohesive failure, but at the same time higher value of  $\sigma_c$  also resists the volume expansion at the interface which increases the difference in the expansion between free surface and the surface attached to the substrate, resulting into buckling effect which eventually initiates the cohesive failure. The tradeoff between these two phenomena can be seen in the Figure 4.7. With lower cohesive strength, tendency of the island to buckle is reduced resulting into delayed crack propagation while higher strength enables structure to withstand deformation of the Si-island for larger expansion, delaying the crack initiation. Here, missing points at lower  $\sigma_c$  with higher value  $G_c$  suggests no crack initiation during the process.

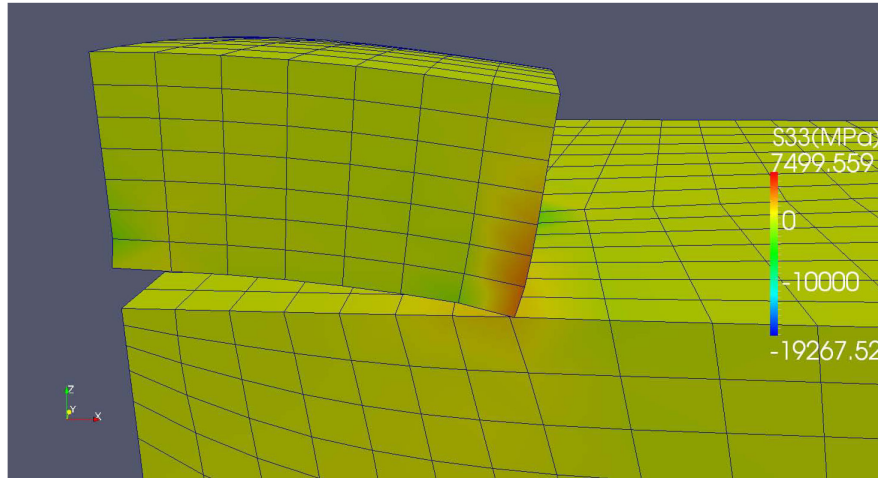


**Figure 4.8:** Buckling of the Si-island because of the intercalation induced volume expansion during lithiation cycle.

Form this study we can conclude that increasing cohesive toughness ensures the stable electrode performance, but increased cohesive strength with constant toughness may increase vulnerability of the structure to some extent. However, lower cohesive strength coupled with higher fracture toughness can suppress the crack altogether, as signified by the missing points. Thus low strength but high energy interfaces may be the best solution for the stability of anode at least when the base material (current collector) is elastic.

## 4.4. Effect of substrate material properties on crack initiation

In this section we will describe the effect of substrate material properties on the crack propagation at the interface. For this study we simulated the problem with various elastic moduli ( $E$ ) of the substrate. In the first case we kept the  $\sigma_c = 1$  GPa constant, and studied the effect of  $E$  at different toughness values as shown in Figure 4.9.

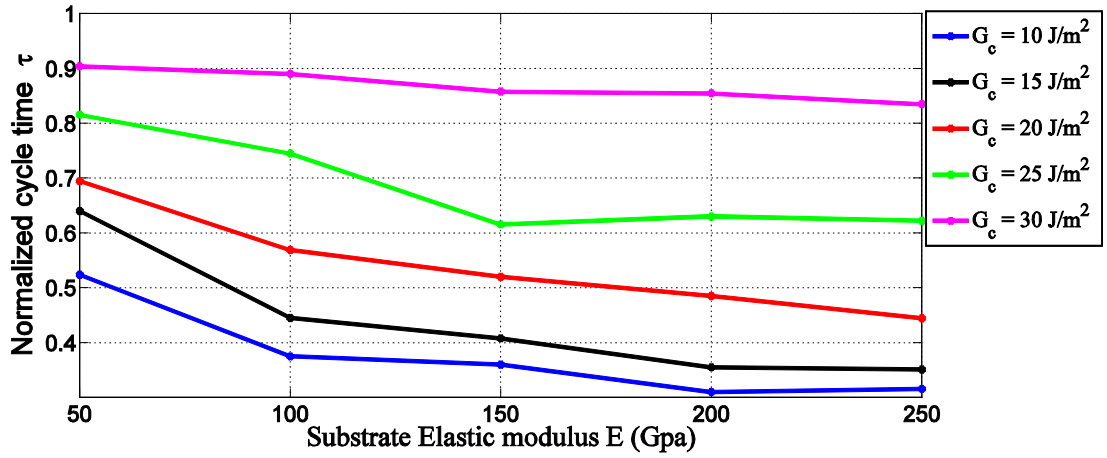


**Figure 4.9:** Time of crack initiation for various elastic moduli ( $E$ ) of substrate and cohesive toughness ( $G_c$ ) considering constant cohesive strength ( $\sigma_c$ ) = 1 GPa.

In the second case we are keeping the value of  $G_c = 20 \text{ J/m}^2$  constant while simulating the effect of elastic modulus for different values of  $\sigma_c$  as show in Figure 4.10.



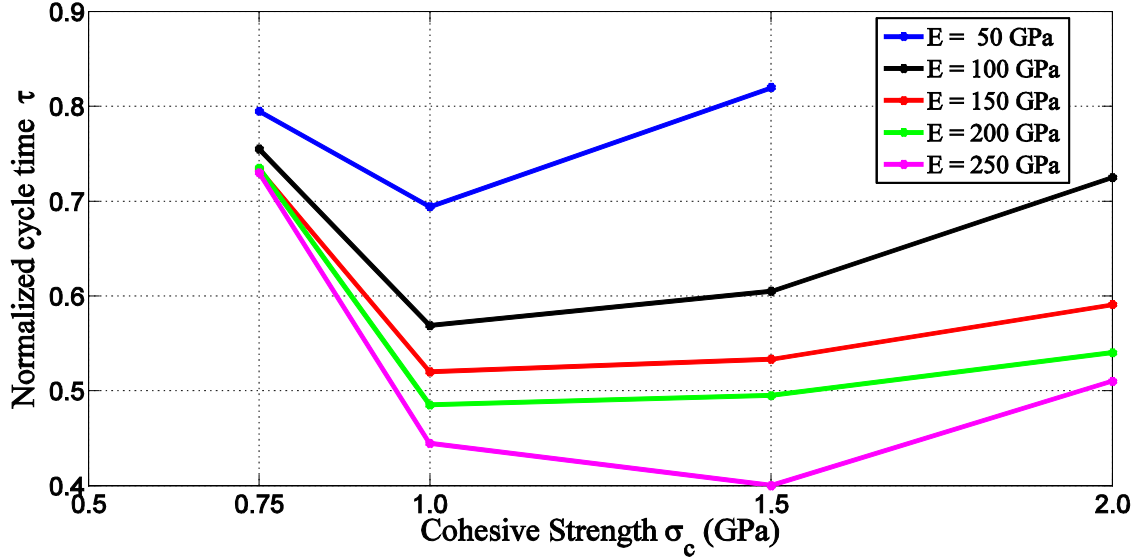


**Figure 4.10:** Time of crack initiation for various elastic moduli ( $E$ ) of substrate and cohesive strength ( $\sigma_c$ ) considering constant cohesive toughness  $G_c = 20 \text{ J/m}^2$ .

In both the studies we can see that, as the elastic modulus of the substrate increases, the interface fails earlier. As also discussed about buckling effect in the previous section for higher cohesive strength, similarly at higher elastic modulus of the substrate, system behaves stiffer and restricts the free expansion of the Si-island increasing the failure tendency while at lower stiffness deformation of the substrates releases the tensile stress at the interface reducing the failure possibilities. Effect of the cohesive strength can also be confirmed from the Figure 4.10 where lower and higher cohesive strength shows delayed crack initiation. The major conclusion from this study is that higher interfacial energy delays the onset of failure as observed in the last section also. Moreover a reduction of elastic mismatch between the substrate and island is also beneficial.

## 4.5. Effect of the plasticity on crack initiation

As the stress in the substrates goes higher than the yield strength of the typical substrate materials like Cu and Al, plastic deformation is unavoidable. In this section, we are

simulating the effect of the plasticity on the crack initiation and comparing it with the results presented in the previous section.

In the first case we are solving the problem with different cohesive strength ( $\sigma_c$ ) values keeping the toughness  $G_c = 10 \text{ J/m}^2$  constant for the interface. Constant elastic modulus  $E = 100 \text{ GPa}$  and yield strength  $\sigma_y = 330 \text{ MPa}$  for the substrate is taken.

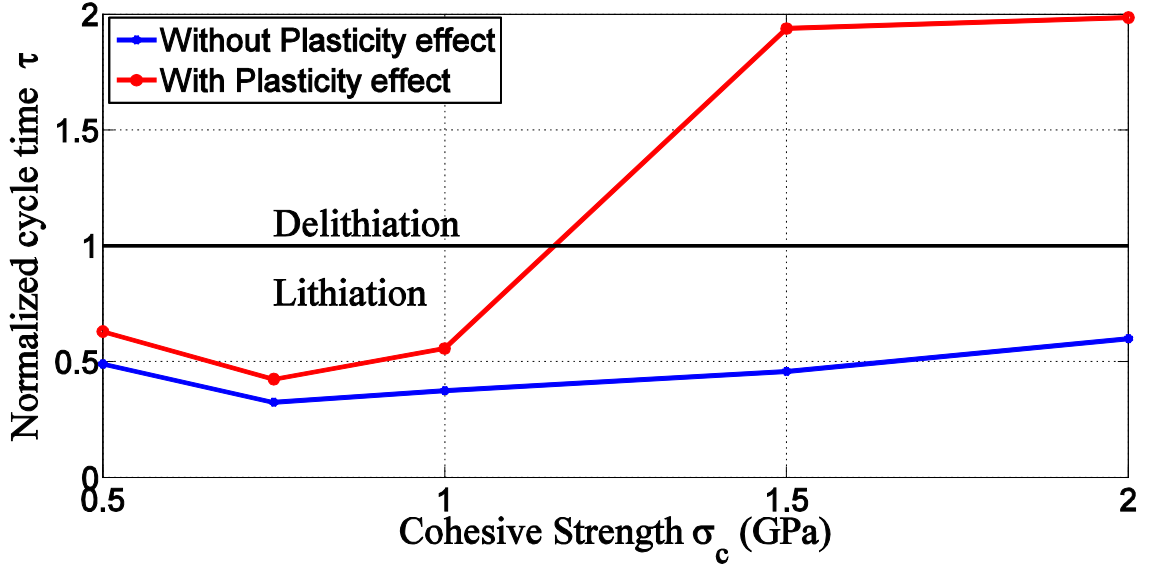


**Figure 4.11:** Comparison of plasticity effect on crack initiation time for various cohesive strengths ( $\sigma_c$ ), considering constant cohesive toughness  $G_c = 10 \text{ J/m}^2$  and constant Elastic modulus of substrate  $E = 100 \text{ GPa}$ .

We can see in Figure 4.11 that, on simulating the plastic deformation in the substrate, crack initiation time increases. Also for the lower cohesive strength crack initiates in the lithiation cycle, while for the higher cohesive strength it initiates during delithiation cycle. In the delithiation cycle failure takes place at the edge of the Si-island which can be attributed to the plastic deformation that occurred during the lithiation. In Figure 4.12 we are comparing the failure mode during lithiation and delithiation cycles. Large amount of plastic deformation appearing close to the edge of the Si-island occurred during volume expansion, which eventually generates tensile stress in the delithiation cycle while island is going back to original configuration and enforces failure.

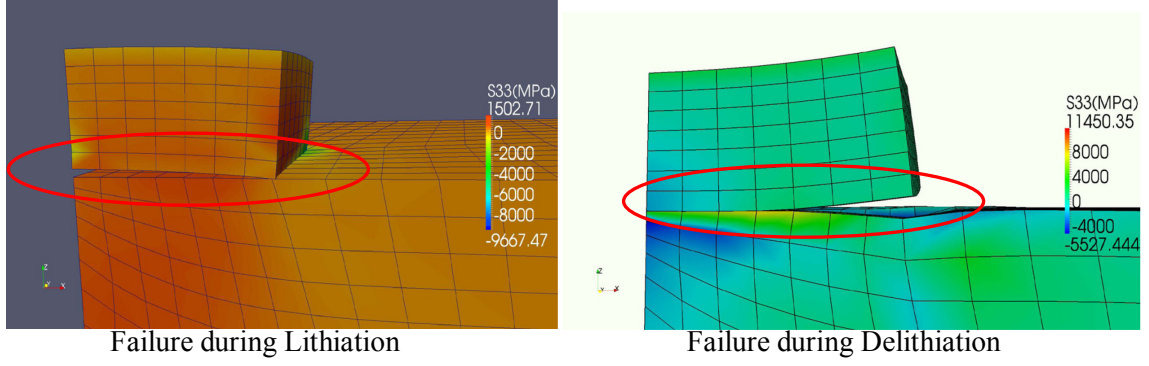


**Figure 4.12:** Comparison of failure mode during Lithiation and Delithiation cycles.

In another study we are considering the effect of various elastic moduli  $E$  and Cohesive toughness  $G_c$  on the crack initiation. In the first case we keep constant cohesive toughness  $G_c = 20 \text{ J/m}^2$  and constant cohesive strength  $\sigma_c = 2.0 \text{ GPa}$  and study the effect of substrate elastic modulus, while in second case we consider the effect of the cohesive toughness on crack initiation keeping constant cohesive strength  $\sigma_c = 2.0 \text{ GPa}$  and elastic modulus of substrate  $E=100 \text{ GPa}$ . Results are presented in the Figure 4.13 and Figure 4.14 considering plastic deformation of the substrate. In this study we can confirm the effect of plasticity as discussed above forcing interface failure in the delithiation cycle by generating tensile stress at the edges. However, on considering the plasticity effect, Elastic modulus has very limited effect on the crack initiation time.

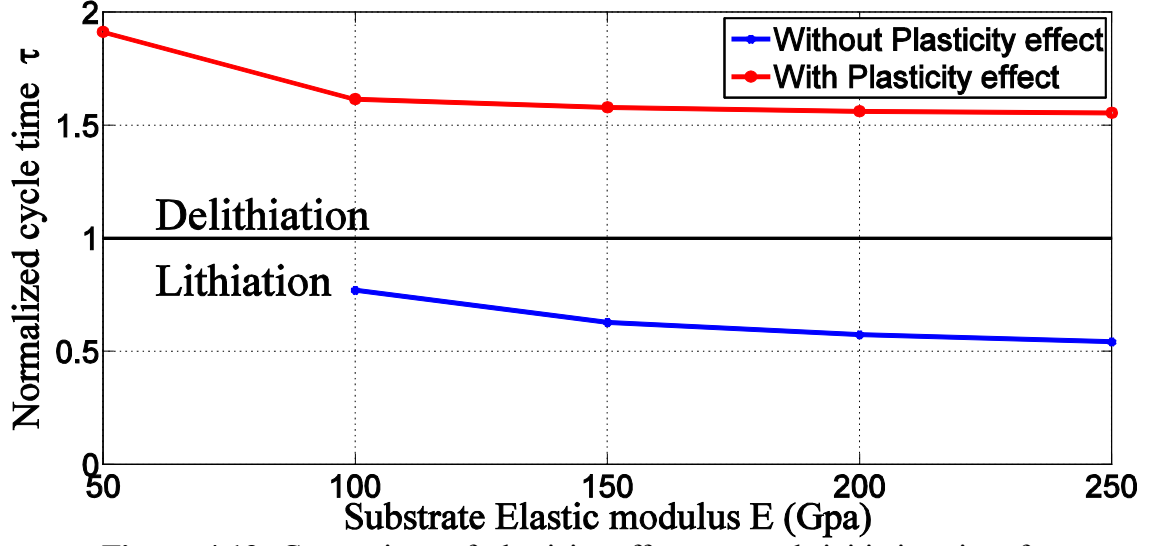


**Figure 4.13:** Comparison of plasticity effect on crack initiation time for various Elastic modulus of substrate  $E$ , considering constant cohesive toughness  $G_c=20 \text{ J/m}^2$  and constant cohesive strength  $\sigma_c = 2 \text{ GPa}$ .

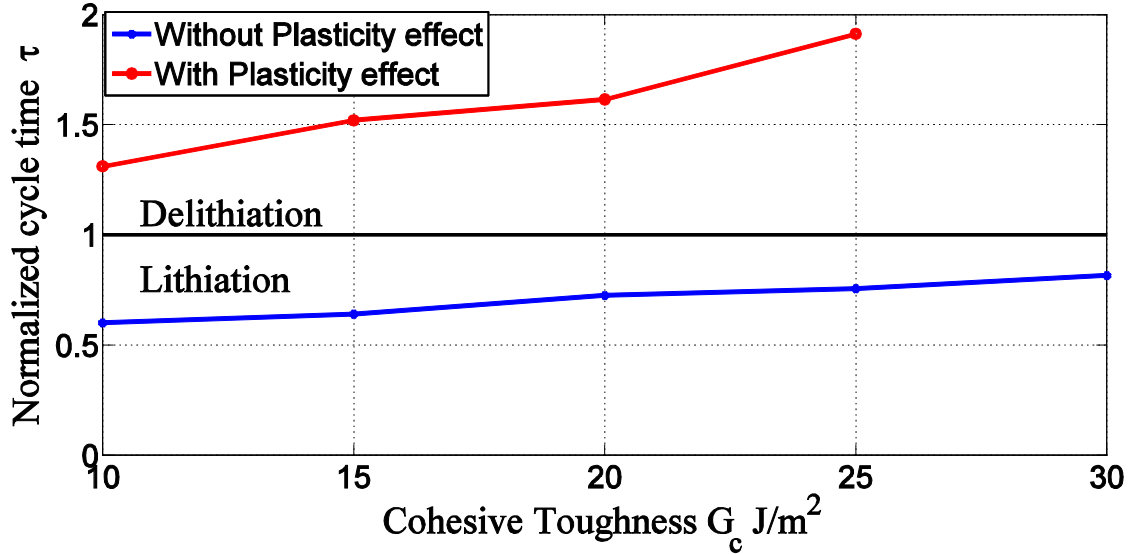


**Figure 4.14:** Comparison of plasticity effect on crack initiation time for various cohesive toughness ( $G_c$ ), considering constant Elastic modulus of substrate  $E = 100 \text{ GPa}$  and constant cohesive strength  $\sigma_c = 2 \text{ GPa}$ .

Evidence of the tensile stress generation at different places due to elastic or plastic deformation of the substrate can be seen in the Figure 4.15 and Figure 4.16. We can see

the stress generated in interface at the middle of the Island in Figure 4.15, which clearly suggests that because of the plastic flow in the substrate tensile stress doesn't reach to the critical strength of the interface hence the failure during lithiation is avoided. Similarly, Figure 4.16 shows high compressive stresses at the corner of the Si-island during lithiation which results in plastic deformation of substrate and eventually generates tensile stress towards the end of delithiation cycle and causes the failure. During lithiation when crack is initiated at the middle of the island, catastrophic failure occurs and complete island gets detached from the substrate, while during delithiation when crack starts from the corner of the island, it stabilizes after some amount of failure.

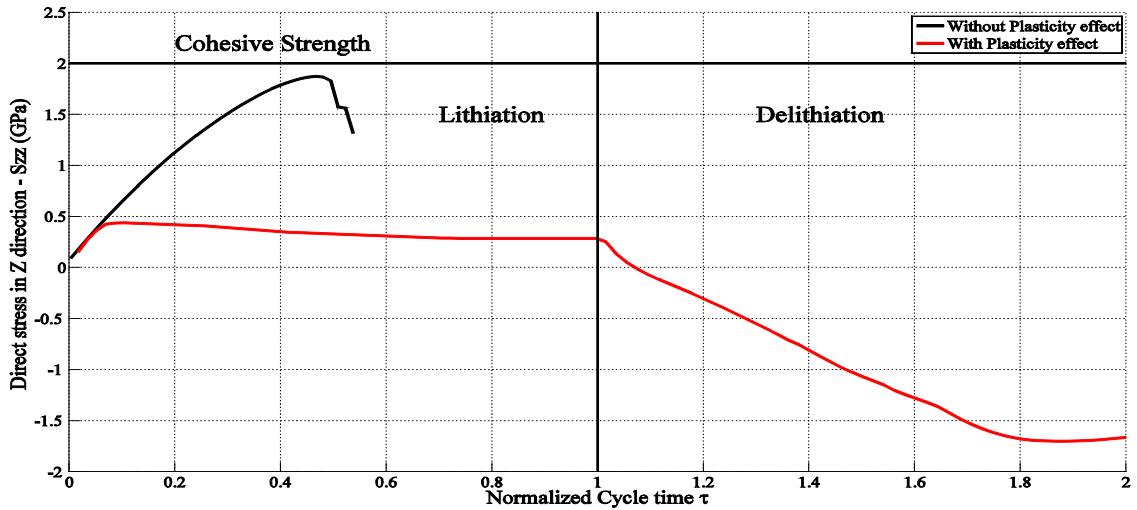


**Figure 4.15:** Comparison of tensile stress generated at the middle of the Si-island considering the plasticity effect

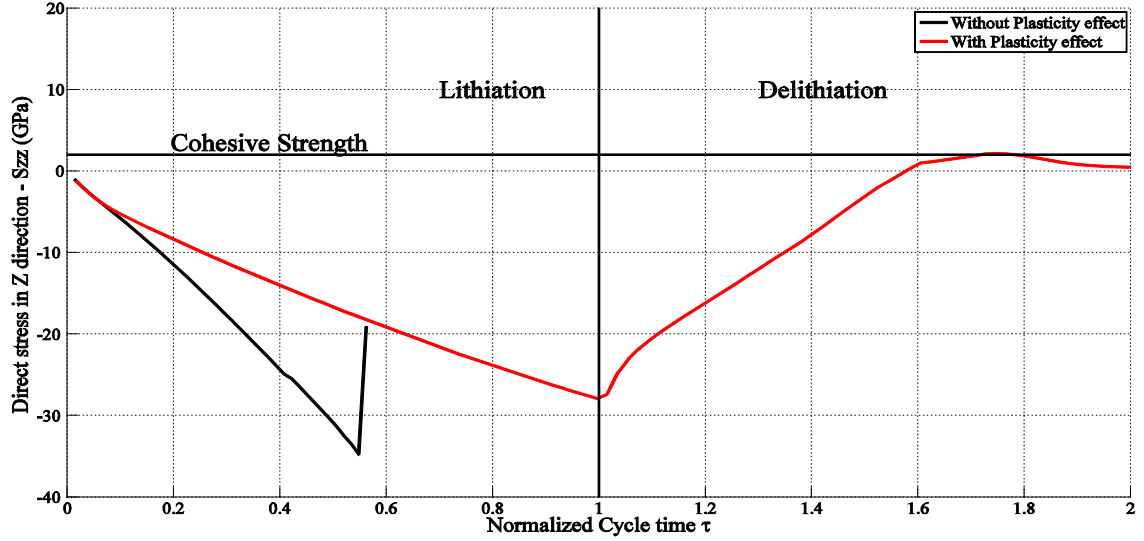


**Figure 4.16:** Comparison of tensile stress generated at the corner of the Si-island considering the plasticity effect

From these studies it can be concluded that the presence of plasticity in the substrate can alter the failure mode significantly. While the failure is in lithiation phase for elastic substrate, plastic effects can shift it to delithiation phase. Also, the crack initiation site is different: for elastic cases it was at the middle of the island while it starts from the corner for plastic case. Also, when the plasticity of the substrate is present, its stiffness does not play a major role in failure of the interface.

# Chapter 5

## Conclusion and Future work

### 5.1. Conclusions

Use of the Si thin film as anode material to develop high performance battery faces many challenges due to large volume expansion associated with the Li-ion intercalation process. To address this problem it is necessary to understand the failure mechanisms and quantify the effect of various parameters affecting. In the present study we proposed a numerical model to study the effect of parameters which has not been addressed yet. In the presented study we have focused on the failure of the interface material between active anode material and the current collector, which is a major contributing factor in the performance degradation due to loss of electrical contact.

In the present study we have solved large deformation problems in three-dimensional domain that proved the importance of considering geometric effect, specifically revealing the buckling effect of the thin film and eventual delamination from the current collector. This phenomenon cannot be demonstrated using single particle 1-D models used in most of the present studies reviewed in Chapter 2. Also the study of material parameters associated with the interface and the substrate has provided interesting results. As expected, higher cohesive toughness gives better stability to the structure, while stiffer substrate materials escalate the crack propagation process. Study also revealed the two way effect of the cohesive strength, and demonstrated effect of stiffer cohesive materials increasing buckling effect which results into early failure during lithiation cycle.

Another major conclusion of the study is the effect of plastic deformation of the substrate. Higher deformation in the substrate after yield stress accommodated the volume expansion of the thin film better delaying and in some case avoiding the crack initiation during lithiation cycle. However, permanent deformation occurring in the

substrate during lithiation also generates tensile stress while Si-thin film trying to attain its original configuration during delithiation process results in the failure at the edges. This phenomenon can answer the stiff capacity degradation in the Si-thin film anode after limited number of cycles.

## **5.2. Future recommendations**

The numerical model presented in this study gives better understanding of the failure mechanisms and reveals previously unknown phenomena affecting the performance degradation. However, the electro-chemical reactions occurring during the process needs to be considered for accurately predict the battery performance in particular operation conditions. As suggested by the experimental study formation of the Solid Electrolyte Interface (SEI) not only resists the diffusion process, but also contributes to the early capacity loss. Thus, the contribution of the SEI should also be included in the numerical study. Another major factor contributing to the failure in subsequent cycles can be the reduction of interfacial cohesive strength due to chemical reactions occurring during Li-ion diffusion. Implementation of the cycle by cycle interface degradation can be useful predicting the crack propagation rate and capacity reduction at each cycle.



# Bibliography

1. Larcher D, Beattie S, Morcrette M, Edstroem K, Jumas JC, Tarascon JM. Recent findings and prospects in the field of pure metals as negative electrodes for Li-ion batteries. *Journal of Materials Chemistry* 2007;17(36):3759-3772.
2. Wei-Jun Z. A review of the electrochemical performance of alloy anodes for lithium-ion batteries. *Journal of Power Sources* 2011;196(1):13-24.
3. Beaulieu LY, Eberman KW, Turner RL, Krause LJ, Dahn JR. Colossal reversible volume changes in lithium alloys. *Electrochemical and Solid State Letters* 2001;4(9):A137-A140.
4. Chunsheng W, Appleby AJ, Kasavajjula U. Nano- and bulk-silicon-based insertion anodes for lithium-ion secondary cells. *Journal of Power Sources* 2007;163(2):1003-39.
5. Zhang XC, Shyy W, Sastry AM. Numerical simulation of intercalation-induced stress in Li-ion battery electrode particles. *Journal of the Electrochemical Society* 2007;154(10):A910-A916.
6. Xiangchun Z, Sastry AM, Wei S. Intercalation-induced stress and heat generation within single lithium-ion battery cathode particles. *Journal of the Electrochemical Society* 2008:A542-52.
7. Park J, Lu W, Sastry AM. Numerical Simulation of Stress Evolution in Lithium Manganese Dioxide Particles due to Coupled Phase Transition and Intercalation. *Journal of the Electrochemical Society* 2011;158(2):A201-A206.
8. Cheng YT, Verbrugge MW. Evolution of stress within a spherical insertion electrode particle under potentiostatic and galvanostatic operation. *Journal of Power Sources* 2009;190(2):453-460.
9. Cheng YT, Verbrugge MW. Diffusion-Induced Stress, Interfacial Charge Transfer, and Criteria for Avoiding Crack Initiation of Electrode Particles. *Journal of the Electrochemical Society* 2010:508-16.
10. Sharma RA, Seefurth RN. Thermodynamic properties of the lithium-silicon system Negative electrodes for secondary cells. 1976 17-22 October; Las Vegas, NV,. *Electrochem. Soc.* p 95-98.
11. Boukamp BA, Lesh GC, Huggins RA. ALL-SOLID LITHIUM ELECTRODES WITH MIXED-CONDUCTOR MATRIX. *Journal of the Electrochemical Society* 1981;128(4):725-729.

12. Dey AN. Electrochemical Alloying of Lithium in Organic Electrolytes. *J. Electrochem. Soc.* 1971;118(10).
13. Winter M, Besenhard JO. Electrochemical lithiation of tin and tin-based intermetallics and composites. *Electrochimica Acta* 1999;45(1-2):31-50.
14. Tirado JL. Inorganic materials for the negative electrode of lithium-ion batteries: state-of-the-art and future prospects. *Materials Science & Engineering R-Reports* 2003;40(3):103-136.
15. Datta MK, Kumta PN. Silicon, graphite and resin based hard carbon nanocomposite anodes for lithium ion batteries. *Journal of Power Sources* 2007;165(1):368-378.
16. Maranchi JP, Hepp AF, Kumta PN. High capacity, reversible silicon thin-film anodes for lithium-ion batteries. *Electrochemical and Solid State Letters* 2003;6(9):A198-A201.
17. Graetz J, Ahn CC, Yazami R, Fultz B. Highly reversible lithium storage in nanostructured silicon. *Electrochemical and Solid State Letters* 2003;6(9):A194-A197.
18. Aurbach D, Baranchugov V, Markevich E, Pollak E, Salitra G. Amorphous silicon thin films as a high capacity anodes for Li-ion batteries in ionic liquid electrolytes. *Electrochemistry Communications* 2007;9(4):796-800.
19. Maranchi JP, Hepp AF, Evans AG, Nuhfer NT, Kumta PN. Interfacial properties of the a-Si/Cu : active-inactive thin-film anode system for lithium-ion batteries. *Journal of the Electrochemical Society* 2006;153(6):A1246-A1253.
20. Park CM, Yoon S, Lee SI, Kim JH, Jung JH, Sohn HJ. High-rate capability and enhanced cyclability of antimony-based composites for lithium rechargeable batteries. *Journal of the Electrochemical Society* 2007;154(10):A917-A920.
21. Kim YU, Lee CK, Sohn HJ, Kang T. Reaction mechanism of tin phosphide anode by mechanochemical method for lithium secondary batteries. *Journal of the Electrochemical Society* 2004;151(6):A933-A937.
22. Hong L, Xuejie H, Liquan C, Zhengang W, Yong L. A high capacity nano-Si composite anode material for lithium rechargeable batteries. *Electrochemical and Solid-State Letters* 1999;2(11):547-9.
23. Takamura T, Saito M, Shimokawa A, Nakahara C, Sekine K, Maeno S, Kibayashi N. Charge/discharge efficiency improvement by the incorporation of conductive carbons in the carbon anode of Li-ion batteries. *Journal of Power Sources* 2000;90(1):45-51.

24. Guo ZP, Wang JZ, Liu HK, Dou SX. Study of silicon/polypyrrole composite as anode materials for Li-ion batteries. *Journal of Power Sources* 2005;146(1-2):448-451.
25. Kim H, Seo M, Park MH, Cho J. A Critical Size of Silicon Nano-Anodes for Lithium Rechargeable Batteries. *Angewandte Chemie-International Edition* 2010;49(12):2146-2149.
26. Yang J, Wang BF, Wang K, Liu Y, Xie JY, Wen ZS. Si/C composites for high capacity lithium storage materials. *Electrochemical and Solid State Letters* 2003;6(8):A154-A156.
27. Il-Seok K, Kumta PN, Blomgren GE. Si/TiN nanocomposites novel anode materials for Li-ion batteries. *Electrochemical and Solid-State Letters*|*Electrochemical and Solid-State Letters* 2000;3(11):493-6.
28. Kim I, Blomgren GE, Kumta PN. Nanostructured Si/TiB<sub>2</sub> composite anodes for Li-ion batteries. *Electrochemical and Solid State Letters* 2003;6(8):A157-A161.
29. Il-seok K, Blomgren GE, Kumta PN. Si-SiC nanocomposite anodes synthesized using high-energy mechanical milling. *Journal of Power Sources* 2004;130(1-2):275-80.
30. Kumta PN, Patel P, Il-Seok K. Nanocomposites of silicon/titanium carbide synthesized using high-energy mechanical milling for use as anodes in lithium-ion batteries. *Materials Science & Engineering B (Solid-State Materials for Advanced Technology)* 2005;116(3):347-52.
31. Wei-Jun Z. A review of the electrochemical performance of alloy anodes for lithium-ion batteries. *Journal of Power Sources* 2011:13-24.
32. Il-Seok K, Kumta PN. High capacity Si/C nanocomposite anodes for Li-ion batteries. *Journal of Power Sources* 2004;136(1):145-9.
33. Datta MK, Kumta PN. Silicon and carbon based composite anodes for lithium ion batteries. *Journal of Power Sources* 2006;158(1):557-563.
34. Guo ZP, Milin E, Wang JZ, Chen J, Liu HK. Silicon/disordered carbon nanocomposites for lithium-ion battery anodes. *Journal of the Electrochemical Society* 2005;152(11):A2211-A2216.
35. Zhang T, Fu LJ, Gao J, Yang LC, Wu YP, Wu HQ. Core-shell Si/C nanocomposite as anode material for lithium ion batteries. *Pure and Applied Chemistry* 2006;78(10):1889-1896.
36. Zuo PJ, Yin GP, Ma YL. Electrochemical stability of silicon/carbon composite anode for lithium ion batteries. *Electrochimica Acta* 2007;52(15):4878-4883.

37. Wang W, Datta MK, Kumta PN. Silicon-based composite anodes for Li-ion rechargeable batteries. *Journal of Materials Chemistry* 2007;17(30):3229-3237.
38. Lee JH, Kim WJ, Kim JY, Lim SH, Lee SM. Spherical silicon/graphite/carbon composites as anode material for lithium-ion batteries. *Journal of Power Sources* 2008;176(1):353-358.
39. Chou SL, Wang JZ, Choucair M, Liu HK, Stride JA, Dou SX. Enhanced reversible lithium storage in a nanosize silicon/graphene composite. *Electrochemistry Communications* 2010;12(2):303-306.
40. Hwang SS, Cho CG, Kim H. Polymer microsphere embedded Si/graphite composite anode material for lithium rechargeable battery. *Electrochimica Acta* 2010;55(9):3236-3239.
41. Prussin S. Generation and Distribution of Dislocations by Solute Diffusion. *Journal of Applied Physics* 1961 32(10).
42. Christensen J, Newman J. A mathematical model of stress generation and fracture in lithium manganese oxide. *Journal of the Electrochemical Society* 2006;153(6):A1019-A1030.
43. Christensen J, Newman J. Stress generation and fracture in lithium insertion materials. *Journal of Solid State Electrochemistry* 2006;10(5):293-319.
44. Verbrugge MW, Cheng YT. Stress and Strain-Energy Distributions within Diffusion-Controlled Insertion-Electrode Particles Subjected to Periodic Potential Excitations. *Journal of the Electrochemical Society* 2009;156(11):A927-A937.
45. Zhao KJ, Pharr M, Vlassak JJ, Suo ZG. Fracture of electrodes in lithium-ion batteries caused by fast charging. *Journal of Applied Physics* 2010;108(7).
46. Zhao KJ, Pharr M, Vlassak JJ, Suo ZG. Inelastic hosts as electrodes for high-capacity lithium-ion batteries. *Journal of Applied Physics* 2011;109(1).
47. Chandrasekaran R, Fuller TF. Analysis of the Lithium-Ion Insertion Silicon Composite Electrode/Separator/Lithium Foil Cell. *Journal of the Electrochemical Society* 2011;158(8):A859-A871.
48. Danilov D, Niessen RAH, Notten PHL. Modeling All-Solid-State Li-Ion Batteries. *Journal of the Electrochemical Society* 2011;158(3):A215-A222.
49. Bhandakkar TK, Huajian G. Cohesive modeling of crack nucleation under diffusion induced stresses in a thin strip: implications on the critical size for flaw tolerant battery electrodes. *International Journal of Solids and Structures* 2010;48:1424-34.

50. Golmon S, Maute K, Dunn ML. Numerical modeling of electrochemical-mechanical interactions in lithium polymer batteries. *Computers & Structures* 2009;1567-79.
51. Christensen J. Modeling Diffusion-Induced Stress in Li-Ion Cells with Porous Electrodes. *Journal of the Electrochemical Society* 2010;157(3):A366-A380.
52. Renganathan S, Sikha G, Santhanagopalan S, White RE. Theoretical Analysis of Stresses in a Lithium Ion Cell. *Journal of the Electrochemical Society* 2010;157(2):A155-A163.
53. Haftbaradaran H, Gao HJ, Curtin WA. A surface locking instability for atomic intercalation into a solid electrode. *Applied Physics Letters* 2010;96(9).
54. Deshpande R, Yue Q, Yang-Tse C. Effects of Concentration-Dependent Elastic Modulus on Diffusion-Induced Stresses for Battery Applications. *Journal of the Electrochemical Society* 2010;967-71.
55. Shenoy VB, Johari P, Qi Y. Elastic softening of amorphous and crystalline Li-Si Phases with increasing Li concentration: A first-principles study. *Journal of Power Sources* 2010;6825-30.
56. Jeon DH, Baek SM. Thermal modeling of cylindrical lithium ion battery during discharge cycle. *Energy Conversion and Management* 2011;52(8-9):2973-2981.
57. Holzapfel GA. *Nonlinear Solid Mechanics. A continuum approach for engineering*. Chichester: John Wiley & Sons Ltd,; 2000.
58. Yang FQ. Interaction between diffusion and chemical stresses. *Materials Science and Engineering a-Structural Materials Properties Microstructure and Processing* 2005;409(1-2):153-159.
59. Ortiz M, Pandolfi A. Finite-deformation irreversible cohesive elements for three-dimensional crack-propagation analysis. *International Journal for Numerical Methods in Engineering* 1999;44(9):1267-1282.
60. Rose JH, Ferrante J, Smith JR. UNIVERSAL BINDING-ENERGY CURVES FOR METALS AND BIMETALLIC INTERFACES. *Physical Review Letters* 1981;47(9):675-678.
61. Camacho GT, Ortiz M. Computational modelling of impact damage in brittle materials. *International Journal of Solids and Structures* 1996;33(20-22):2899-2938.
62. Maiti S, Geubelle PH. A cohesive model for fatigue failure of polymers. *Engineering Fracture Mechanics* 2005;72(5):691-708.

63. Callister WD, Rethwisch DG. Materials Science and Engineering: An Introduction. John Wiley & Sons; 2009.
64. Nishikawa K, Fukunaka Y, Sakka T, Ogata YH, Selman JR. Ionic mass transfer during electrochemical dissolution of Li metal in PC electrolyte solution. Journal of Electroanalytical Chemistry 2005;584(1):63-69.
65. Boley BA, Weiner JH. Theory of Thermal Stress. New York: John Wiley & Sons; 1960. 586 p.

# Appendix A

## A.1 Tensorial notations

Let us assume  $\mathbf{A}$  and  $\mathbf{B}$  are 2nd order tensor, and  $\mathbf{C}$  and  $\mathbf{D}$  be the 4th order tensors, the tensorial representations and their useful properties are as follows:

$$\mathbf{AB} = A_{ik} B_{kj} \quad (\text{A.1})$$

$$\mathbf{A} \otimes \mathbf{B} = A_{ij} B_{kl} \quad (\text{A.2})$$

$$\mathbf{A} : \mathbf{B} = A_{ij} B_{ij} \quad (\text{A.3})$$

$$\mathbf{C} : \mathbf{A} = C_{ijmn} A_{mn} \quad (\text{A.4})$$

$$\mathbf{C} : \mathbf{D} = C_{ijmn} D_{mnkl} \quad (\text{A.5})$$

$$\text{tr} \mathbf{A} = \mathbf{A} : \mathbf{I} = A_{ii} \quad (\text{A.6})$$

$$\left( \frac{\partial \mathbf{A}^{-1}}{\partial \mathbf{A}} \right)_{ijkl} = -\frac{1}{2} (A_{ik}^{-1} A_{lj}^{-1} A_{il}^{-1} A_{kj}^{-1}) \quad (\text{A.7})$$

## A.2 Finite element matrices

The components of matrix  $\mathbf{K}_c$  in Equation (25) are given as

$$\mathbf{K}_c = \mathbf{K}_{c1} + \mathbf{K}_{c2} + \mathbf{K}_{c3} + \mathbf{K}_{c4} \quad (\text{A.8})$$

where,

$$\mathbf{K}_{c1} = \sum_{e=1}^{n_{el}} \int_{\Omega_0^e} \frac{\mathbf{N}_c^T \mathbf{N}_c}{\Delta t} \partial \Theta \quad (\text{A.9})$$

$$\mathbf{K}_{c2} = \sum_{e=1}^{n_{el}} \int_{\Omega_0^e} \mathbf{B}_c^T D \mathbf{B}_c \partial \Theta \quad (\text{A.10})$$

$$\mathbf{K}_{c3} = - \sum_{e=1}^{n_{el}} \int_{\Omega_0^e} \mathbf{B}_c^T \frac{D\eta}{RT} \nabla p_k^{n+1} \mathbf{N}_c \partial \Theta \quad (\text{A.11})$$

$$\mathbf{K}_{c4} = - \sum_{e=1}^{n_{el}} \int_{\Omega_0^e} \mathbf{B}_c^T \frac{D\eta c_k^{n+1}}{RT} \nabla \left( \frac{\partial p^{n+1}}{\partial c^{n+1}} \right)_k \mathbf{N}_c \partial \Theta \quad (\text{A.12})$$

The component of residuals in Equation (25) are given as

$$\mathbf{R}_c = \mathbf{R}_{c1} + \mathbf{R}_{c2} + \mathbf{R}_{c3} + \mathbf{R}_{c4} \quad (\text{A.13})$$

where,

$$\mathbf{R}_{c1}^k = \sum_{e=1}^{n_{el}} \int_{\partial \Omega_0^e} \mathbf{N}_c^T J_0^{n+1} \partial \Gamma \quad (\text{A.14})$$

$$\mathbf{R}_{c2}^k = - \sum_{e=1}^{n_{el}} \int_{\Omega_0^e} \mathbf{N}_c^T \mathbf{N}_c \partial \Theta \left\{ \frac{\bar{c}_k^{n+1} - \bar{c}^n}{\Delta t} \right\} \quad (\text{A.15})$$

$$\mathbf{R}_{c3}^k = - \sum_{e=1}^{n_{el}} \int_{\Omega_0^e} \mathbf{B}_c^T D \mathbf{B}_c \partial \Theta \bar{c}_k^{n+1} \quad (\text{A.16})$$

$$\mathbf{R}_{c4}^k = \sum_{e=1}^{n_{el}} \int_{\Omega_0^e} \mathbf{B}_c^T \frac{D\eta}{RT} \nabla p_k^{n+1} \mathbf{N}_c \partial \Theta \bar{c}_k^{n+1} \quad (\text{A.17})$$



### A.3 Matrix manipulation

$$\mathbf{F}_\theta^{-T} = \mathbf{F}_\theta^{-1} \quad (\text{A.18})$$

$$\nabla J_\theta = \eta \nabla c \quad (\text{A.19})$$

$$\frac{\partial J_\theta}{\partial c} = \eta \quad (\text{A.20})$$

$$\frac{\partial \mathbf{F}_\theta}{\partial J_\theta} = \frac{1}{3} J_\theta^{-\frac{2}{3}} \mathbf{I} \quad (\text{A.21})$$

$$\frac{\partial \mathbf{F}_\theta}{\partial c} = \frac{1}{3} \eta J_\theta^{-\frac{2}{3}} \mathbf{I} \quad (\text{A.22})$$

$$\begin{aligned} \nabla p_k^{n+1} = & -\frac{2}{9} \eta J_\theta^{-\frac{5}{3}} \text{tr}(\mathbf{M}_e \mathbf{F}_\theta^{-1}) \nabla c_k^{n+1} \\ & + \frac{1}{3} \eta J_\theta^{-\frac{2}{3}} \text{tr} \left[ \mathbf{M}_e \left[ \frac{\partial \mathbf{F}_\theta^{-1}}{\partial \mathbf{F}_\theta} : \frac{\partial \mathbf{F}_\theta}{\partial J_\theta} \right] \right] \nabla c_k^{n+1} \end{aligned} \quad (\text{A.23})$$

$$\begin{aligned} \frac{\partial p_k^{n+1}}{\partial c^{n+1}} = & -\frac{2}{9} \eta J_\theta^{-\frac{5}{3}} \text{tr}(\mathbf{M}_e \mathbf{F}_\theta^{-1}) \\ & + \frac{1}{3} J_\theta^{-\frac{2}{3}} \text{tr} \left[ \mathbf{M}_e \left[ \frac{\partial \mathbf{F}_\theta^{-1}}{\partial \mathbf{F}_\theta} : \frac{\partial \mathbf{F}_\theta}{\partial c} \right] \right] \end{aligned} \quad (\text{A.24})$$

# Appendix B

## Copyright permission for Figure 1.3

Dear Dr Patel

The Royal Society of Chemistry hereby grants permission for the use of the material specified below in the work described and in all subsequent editions of the work for distribution throughout the world, in all media including electronic and microfilm. You may use the material in conjunction with computer-based electronic and information retrieval systems, grant permissions for photocopying, reproductions and reprints, translate the material and to publish the translation, and authorize document delivery and abstracting and indexing services. The Royal Society of Chemistry is a signatory to the STM Guidelines on Permissions (available on request).

Please note that if the material specified below or any part of it appears with credit or acknowledgement to a third party then you must also secure permission from that third party before reproducing that material.

Please ensure that the published article carries a credit to The Royal Society of Chemistry in the following format:

*[Original citation] – Reproduced by permission of The Royal Society of Chemistry*

and that any electronic version of the work includes a hyperlink to the article on the Royal Society of Chemistry website. The recommended form for the hyperlink is <http://dx.doi.org/10.1039/DOI suffix>, for example in the

link <http://dx.doi.org/10.1039/b110420a> the DOI suffix is 'b110420a'. To find the relevant DOI suffix for the RSC paper in question, go to the Journals section of the website and locate your paper in the list of papers for the volume and issue of your specific journal. You will find the DOI suffix quoted there.

Regards

Gill Cockhead

Contracts & Copyright Executive

Gill Cockhead (Mrs), Contracts & Copyright Executive

Royal Society of Chemistry, Thomas Graham House

Science Park, Milton Road, Cambridge CB4 0WF, UK

Tel +44 (0) 1223 432134, Fax +44 (0) 1223 423623

<http://www.rsc.org>

---

Name : Siddharth H Patel

Address :

1801 E Woodmar Drive,

Houghton,

MI - 49931

USA

Tel : 2488855909

Fax :

Email : [shpatell@mtu.edu](mailto:shpatell@mtu.edu)

I am preparing the following work for publication:

Article/Chapter Title : Numerical modeling of the failure mechanisms in Si thin film anode for Li-ion batteries

Journal/Book Title : NA / Thesis

Editor/Author(s) : Siddharth Patel

Publisher : Michigan Technological University and ProQuest/UMI

I would very much appreciate your permission to use the following material:

Journal/Book Title : Journal of Materials Chemistry

Editor/Author(s) : Dominique Larcher, Shane Beattie, Mathieu Morcrette, Kristina Edström, Jean-Claude Jumas and Jean-Marie Tarascon

Volume Number : 17

Year of Publication : 2007

Description of Material : Recent findings and prospects in the field of pure metals as negative electrodes for Li-ion batteries : (Figure 1)

Page(s) : 3759-3772

Any Additional Comments :

Respected Sir/Madam,

I am writing an Master's Thesis, where I want to reproduce the Figure 1. of the above mentioned review paper from the Journal of Materials Chemistry. I would request you to grant me the permission for the same.

Regards,

Siddharth Patel

# Appendix C

## Copyright permission for Figure 2.1

### Request for Permission to Reproduce or Re-Publish ECS Material

Please fax this form to: The Electrochemical Society (ECS), Attn: Permissions Requests, 1.609.730.0629.  
You may also e-mail your request to: [copyright@electrochem.org](mailto:copyright@electrochem.org). Include all the information as required on this form. Please allow 3-7 days for your request to be processed.

I am preparing a (choose one): ☐ paper ☐ chapter ☐ book ☒ thesis

entitled: Numerical modeling of the failure mechanisms in Si thin film anode for Li-ion batteries

to be published by: Michigan Technological University and ProQuest/UMI

in an upcoming publication entitled: \_\_\_\_\_

I request permission to use the following material in the publication noted above, and request nonexclusive rights for all subsequent editions and in all foreign language translations for distribution throughout the world.

**Description of material to be used**—Indicate what material you wish to use (figures, tables, text, etc.) and give the full bibliographic reference for the source publication. You may attach a separate list, organized by ECS title.

I request a permission to reproduce the Figure 4 and Figure 6(b) from the article,  
Maranchi, J.P., A.F. Hepp, and P.N. Kumta, *High capacity, reversible silicon thin-film anodes for lithium-ion batteries*. Electrochemical and Solid State Letters, 2003. 6(9): p. A198-A201.

Signature: \_\_\_\_\_ Date: August 1, 2011

Name: Siddharth Patel

Address: 1801 E Woodmar Drive,

Houghton,

MI-49931, USA

Telephone: 01-248 885 5909 Fax: \_\_\_\_\_

E-mail: shpatel1@mtu.edu

Permission is granted to reproduce the above-referenced material. Please acknowledge the author(s) and publication data of the original material, and include the words: "Reproduced by permission of The Electrochemical Society."

Aug. 5, 2011  
Date

\_\_\_\_\_  
Ann F. Goedkoop, Director of Publications